Determining thermal inertia of eclipsing binary asteroids: the role of shape

Marlies van de Weijgaert

Kapteyn Astronomical Institute, University of Groningen, The Netherlands

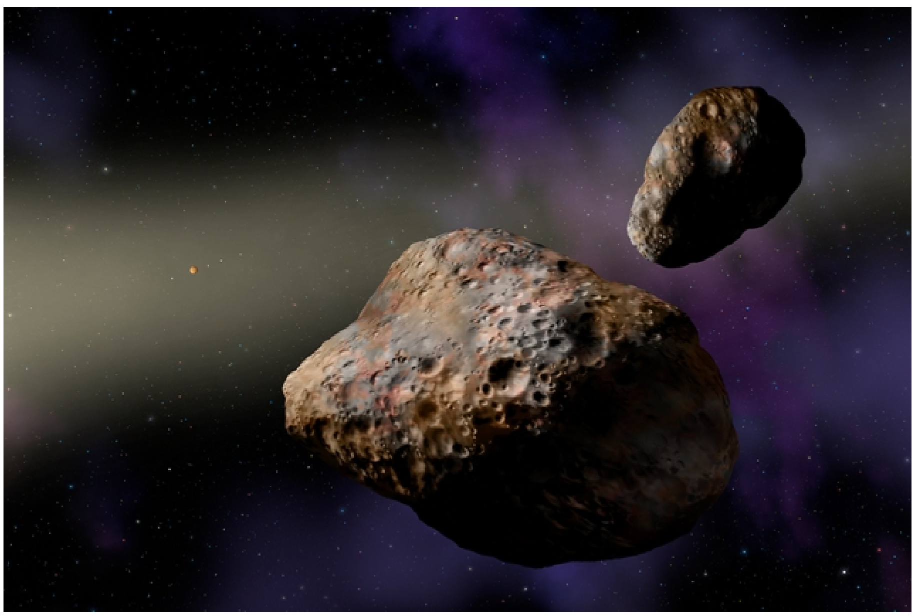

Report Master Research

Supervisors:
Dr. M. Mueller
Prof. dr. F. van der Tak

Groningen, April 2017

Cover figure

Artist's impression of the binary asteroid 617 Patroclus, a Trojan asteroid gravitationally locked to trail 60° behind Jupiter in its orbit around the Sun. The two components in this system are similar in size and ellipsoidal in shape. Image credit: Lynette Cook and W. M. Keck Observatory.

Abstract

The physical and dynamical properties of asteroids are windows into the complex history of the solar system. Of particular interest is the thermal inertia of asteroids, a very sensitive indicator for the looseness of surface material: mature, fine-grained regolith has a much lower thermal inertia than compact material.

Knowledge of thermal inertia aids the planning of spacecraft operations near or on asteroid surfaces. Through the Yarkovsky effect, thermal inertia can measurably influence asteroid orbits and plays a crucial role in the prediction and prevention of asteroid impacts on Earth.

The topic of this work is to study the role of component shape in the analysis of the thermal emission of eclipsing binary asteroids. This method was pioneered by Mueller et al. (2010) with Spitzer IRS observations of eclipses in the binary Trojan asteroid system (617) Patroclus-Menoetius. Their analysis yielded the first direct measurement of asteroid thermal inertia and the first determination of this property for a Trojan asteroid.

Based on the evidence available at the time, Mueller et al. (2010) assumed spherical component shapes. However, Buie et al. (2015) derived a significantly ellipsoidal shape through occultation observations. We reanalyze the Spitzer observations of Patroclus using that shape as an input parameter. We also employed other shape models, interpolating between the sphere and the Buie et al. shape model as well as extrapolating beyond it, in order to study the influence of component shape.

We find component shape to have a dramatic impact on the thermal emission of eclipsing binary asteroids. As a consequence, we find thermal-inertia values that are reduced by factors of several J $s^{-1/2}$ K^{-1} m^{-2}. For one eclipse event ('event 1'), we find 0.23 $\pm$ 0.17 J $s^{-1/2}$ K^{-1} m^{-2} while Mueller et al. found 21 $\pm$ 14 J $s^{-1/2}$ K^{-1} m^{-2}. For the other eclipse event ('event 2'), we find 1.00 $\pm$ 0.45 J $s^{-1/2}$ K^{-1} m^{-2} while Mueller et al. found 6.4 $\pm$ 1.6 J $s^{-1/2}$ K^{-1} m^{-2}.

Our thermal-inertia result is at the low edge of the plausible range and indicates extreme looseness in the topmost surface layer. The two events are representative of the thermal inertia of the two separate components of the Patroclus system. If the two components are formed from the same material, one would expect them to display identical thermal inertia. The comparison between the thermal inertia for events 1 and 2 does not support nor reject this possibility.

These results will support further studies into the thermal properties, composition and structure of asteroids. Patroclus, our target asteroid, is also among the targets of the Lucy mission, currently under study at NASA. If approved, Lucy will fly by Patroclus in 2033, providing highly resolved data.

Contents

Chapter 1

Introduction

Asteroids or minor planets are small bodies in the solar system in direct orbit around the Sun that are not planets or moons and do not show any active comet characteristics. They are the remnants of the formation of the solar system in the sense that they did not become part of the central star or one of the planets. Many of them are probably fragments of collided planetesimals that did not grow to the size of a protoplanet or planet. They can be as small as dust grains or larger. The largest known asteroid is Ceres with a diameter of almost 1000 km, which is also classified as a dwarf planet and possibly a surviving protoplanet.

Since most asteroids have undergone much less processing since their formation than the Sun and planets, they contain information on the early formation stage of our solar system. The distribution of asteroids throughout the solar system and their physical properties also provide clues about the solar system's evolution. Knowledge of our own planetary system will aid the understanding of other planetary systems in modeling them and interpreting their observational data.

1.1 Dynamical classes of asteroids

There are millions of asteroids in the solar system. They can be divided in dynamical asteroid groups that share similar orbits. Some asteroids have a common origin such as the fragmentation of a single asteroid due to a collision in the past (see Figure 1.1). Most of the asteroids in the solar system are main-belt asteroids (MBAs) between the orbits of Mars and Jupiter. Orbital resonances with Jupiter divide this asteroid group in an inner main belt (<2.5 AU), a middle main belt (2.5-2.8 AU) and an outer main belt (>2.8 AU). Almost as numerous are the Jupiter Trojan asteroids (see Sect. 1.2) that librate around gravitational stability points within the orbit of Jupiter.

Of particular relevance to mankind are the near-Earth asteroids (NEAs). As their name implies, these come closer to Earth and may cross its orbit or even be potentially hazardous and strike the Earth. Unlike most natural disasters, an asteroid impact is a predictable and theoretically preventable event, if we have sufficient knowledge on the asteroid orbital parameters. Determining this as accurately and for as many NEAs as possible is an ongoing effort.

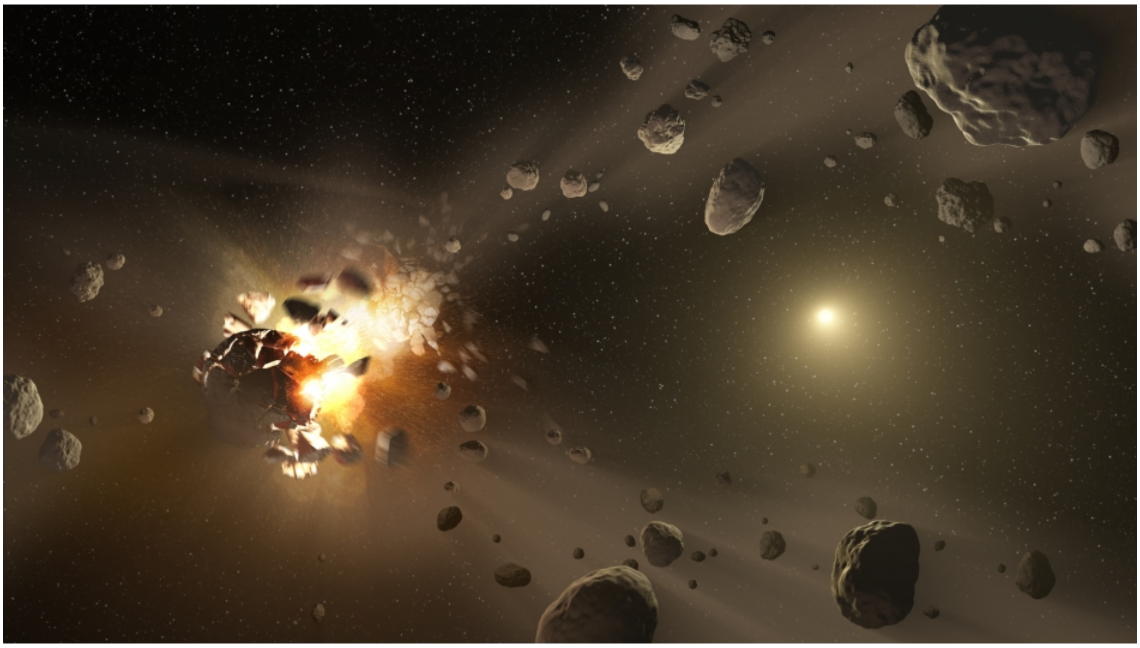

Figure 1.1: An artist's conception how a family of asteroids is created in a collision. Image credit: NASA/JPL-Caltech.

1.2 Jupiter Trojans

617 Patroclus, the target of this research, is a Jupiter Trojan. The Jupiter Trojans are trapped into two gravitationally stable regions of the Sun-Jupiter system, called the Jupiter Lagrangian L_4 and L_5 points. These points lie along the orbit of Jupiter, so the Jupiter Trojans accompany Jupiter in its orbit around the Sun. The Greek camp leads the way $60°$ ahead of Jupiter at the Lagrangian L_4 point and the Trojan camp trails $60°$ behind at the Lagrangian L_5 point. Also see Figure 1.2 for an illustration.

Trojan asteroids have dark surfaces with almost featureless, reddish spectra. They may be coated in a mixture of fine silicates grains, possibly organic compounds and other opaque materials.

The origin of the Trojans is under debate. They may have formed at the present location in the solar nebula, or may have been formed at a different location and been captured in the Lagrangian points during a migration, or a combination of both.

Statistical analysis of colors and spectra of Trojan asteroids separates them into two separate spectral groups. One group has a reddish spectrum (referred to as D-type asteroid) and the other group has a less-red spectrum (referred to as P-type asteroid). Emery et al. (2011) suggest that the redder group may have formed farther out in the solar system and was captured in the Jupiter Lagrangian points after a chaotic phase in the solar system evolution as described in the Nice model by Morbidelli et al. (2005), and that the less-red group originated near Jupiter or in the main asteroid belt.

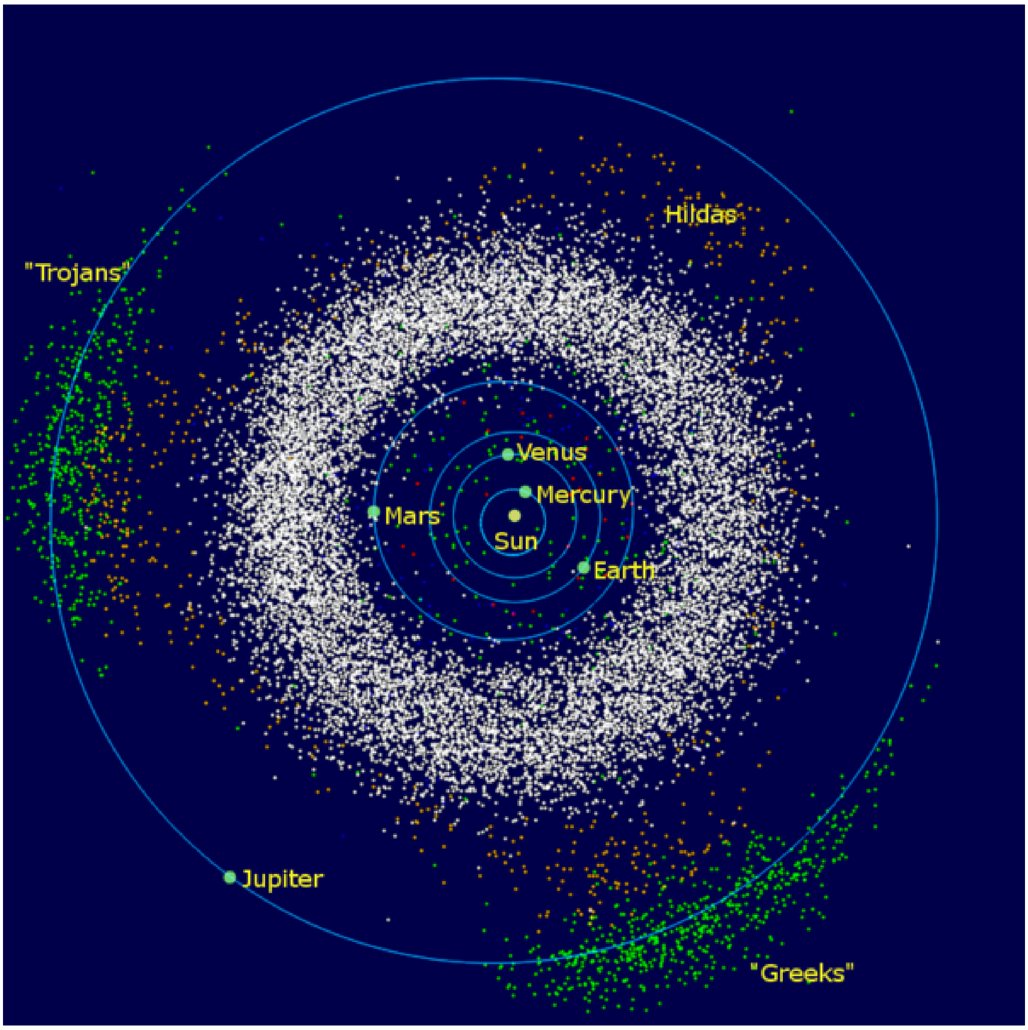

Figure 1.2: The inner solar system, from the Sun to the orbit of Jupiter. The main asteroid belt between the orbits of Mars and Jupiter is indicated in white dots. Green dots represent Jupiter Trojans, in a leading 'Greek' and trailing 'Trojan' camp. The orange dots are the Hilda asteroids, another dynamical group of asteroids in a 3:2 orbital resonance with Jupiter. More smaller of such dynamical groups exist as well, this figure does not include all asteroid groups in the solar system. Figure from `https://en.wikipedia.org/wiki/Jupiter_trojan`.

Only two binaries are currently known among the Trojans, our target 617 Patroclus is one of them. The apparent lack of binary Trojans is intriguing and may give clues about their formation history. Possibly only close or contact binaries were able to stay gravitationally bound in the chaotic period before their capture in a Lagrangian point (Margot et al., 2015). But there is no conclusive evidence yet, and the origin of Trojans remains a topic of active research.

1.3 Asteroid taxonomy

The compositions of asteroid surfaces are mainly derived from their visible and near-IR spectra. This divides asteroids in a few characteristic classes, of which we will name the main ones.

C-type asteroids are carbon-rich asteroids and seem to represent the majority of outer main belt objects. S-type asteroids are silicate-rich or stony and dominate the inner main belt and NEA realm. M-type asteroids are moderately bright and are generally identified with a pure or partial metallic nickel-iron composition, but can also be non-metallic.

Most Trojans are of D-type or P-type. P-type asteroids have a low albedo and may contain organic rich silicates, perhaps with water ice interiors. D-type asteroids have a similarly low albedo and roughly the same composition as the P-types, but a distinctly redder spectrum. This may indicate different ratios of the compositional elements and possibly a different origin (Emery et al., 2011).

1.4 Thermal inertia

Thermal inertia is the resistance of a physical object to a change in its surface temperature. It is thus the thermal variant of inertia, which is the resistance of a physical object to a change in its motion. Thermal inertia measures how slowly a body reaches the same temperature as its surroundings. This depends on a combination of physical properties as discussed below.

A conductive material like a metal will transport and distribute heat quickly to its interior. The surface will therefore not become significantly warmer than the inside. The surface temperature takes more effort to increase in this case, giving a high thermal inertia. On the other hand, an insulating material like dust or foam will strongly resist a temperature change. The heat cannot penetrate the material and builds up on the surface. The surface temperature is thus easy to increase, giving a low thermal inertia. In between these extremes is a whole spectrum of materials with varying thermal inertia depending on their density, specific heat and ability to conduct heat.

A high thermal inertia thus keeps the surface temperature low for a long time. A high thermal inertia like metal therefore feels cooler than the surrounding temperature at first touch. And on a hot day at the beach a dive in the sea water with medium high thermal inertia will feel refreshingly cool after walking on the hot beach sand with its lower thermal inertia.

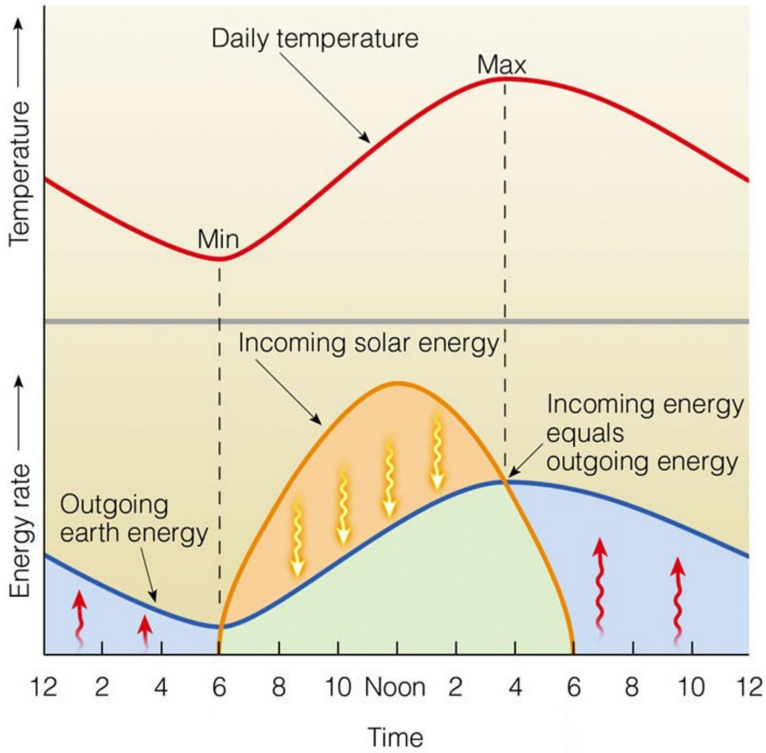

Figure 1.3: Example of thermal inertia in relation with the daily temperature variation on Earth. The top panel shows the surface temperature as a function of time during the day, the bottom diagram plots the incoming and outgoing energy during a day. The daily temperature is controlled by the incoming solar radiation and outgoing infrared radiation. Thermal inertia determines how fast the surface temperature rises and falls. Since the surface stays warm for some time, the maximum temperature is lagging behind on the solar maximum. Figure from `http://www.atmos.washington.edu/~hakim/101/101.cgi`.

Another example of thermal inertia is given in Figure 1.3. The Earth is constantly releasing heat with outgoing infrared radiation. Heat is mainly incoming from solar radiation during the day. The incoming energy causes the Earth's surface to rise in temperature. How fast this happens depends on the thermal inertia of the surface. When the incoming solar energy drops below the outgoing infrared radiation, the temperature of the Earth's surface decreases again. Note that, due to thermal inertia, the highest temperature does *not* occur at noon but a few hours later. This is the basis of the Yarkovsky effect, see Sect. 2.4.

1.5 This research

The thermal inertia of an asteroid gives insight into its surface structure. It can be determined by studying the thermal response of the asteroid surface to a temperature change of the surroundings. An eclipse event in a binary asteroid system offers the opportunity to measure thermal inertia directly in one single event. Mueller et al. (2010) were the first to apply this method to eclipses in the binary Trojan asteroid system (617) Patroclus using Spitzer IRS observations. This was also the first determination of thermal inertia for a Trojan asteroid.

The analysis by Mueller et al. (2010) assumed a spherical shape for both components of Patroclus. However, stellar occultation observations by Patroclus from Buie et al. (2015) revealed that the components are more ellipsoidal. Given that the shape of the asteroid changes the configuration of an eclipse and thus the shadows and temperature variations on the surface, the shape is expected to influence the determination of thermal inertia. In this research, we refine the analysis of the thermal eclipse data with the new shape model and investigate the influence of asteroid shape in the thermophysical eclipse model using the existing Spitzer data.

In chapter 2 we will first give an introduction to thermal inertia of asteroids, describe how we measure the thermal inertia of asteroids with a thermophysical model and discuss some implications of this property.

In chapter 3, we introduce our target asteroid, the Trojan binary system 617 Patroclus-Menoetius. We will describe the observations of two mutual eclipse events in the Patroclus system that were performed by Mueller et al. (2010) to determine its thermal inertia.

In chapter 4 we set out the steps for the data analysis, starting with an illustration of the implemented ellipsoid asteroid models, followed by the reanalysis of the Patroclus eclipse events with these improved asteroid shapes.

Finally, chapter 5 and 6 contain the discussion of the results and conclusions of this research.

Chapter 2

Thermal inertia of asteroids

We will first describe how we measure the thermal inertia of asteroids, and explain the theory of the thermophysical model that is used in this research. Then we give some examples of thermal inertia values for different materials and asteroids, and mention a few applications that motivate the study of thermal inertia of asteroids.

2.1 Measuring thermal inertia

To measure the resistance of a material to temperature changes, we need to monitor the material while it is undergoing these changes. An object in space does continuously experience temperature changes when it is warmed by a heat source from one direction while it rotates around its axis. In our solar system the Sun is the main heat source and rotating objects cycle through alternating day and night phases. In theory we can observe a rotating asteroid from different angles to see its dayside and nightside. The thermal inertia can then be inferred from the asteroid's diurnal temperature variation.

Ideally you would want to measure the temperature on consecutive days and nights, but in practice these observations have to be spaced with long time intervals. Normally you do not have the luxury to orbit an asteroid, but you observe it from a long distance and the rotational phase from your point of view changes slowly.

Another type of event that causes a temperature change is an eclipse, when one object moves in front of the Sun as seen from another object. The first object blocks the sunlight which causes the temperature on the second object to drop. A realtime eclipse enables a direct and immediate detection of temperature changes. Eclipses can occur between any types of objects in space. Solar eclipses and lunar eclipses are the best known types, but an eclipse can also occur between other planets and their moons, binary stars and even binary asteroids.

Pettit and Nicholson were the first to measure the thermal inertia of the Moon with this technique during a total lunar eclipse (Pettit and Nicholson, 1930). The technique has also been applied to eclipses of other natural satellites by their host planet, such as Jupiter and Saturn and even by Saturn's rings (Morrison and Cruikshank, 1973; Neugebauer et al., 2005; Pearl et al., 2008).

In general eclipses occur much more frequently and regularly between mutually orbiting objects than for single objects. Single asteroids in space are also not frequently eclipsed and certainly not regularly. But in a binary asteroid system both components can alternately eclipse each other. More and more binary asteroids are now known in which mutual eclipse events can be quite accurately predicted (see Mueller et al., 2010). In this research we analyze observations of the binary asteroid system 617 Patroclus during eclipse events in June 2006.

The eclipse method allows for a direct measurement of thermal inertia of binary asteroids. However, this technique cannot be used for all asteroids. The diurnal method will still be useful for more statistically significant data. The different methods are complimentary to each other.

2.2 Thermophysical model

In a thermophysical model (TPM), the surface of an asteroid is modeled by a mesh of triangular facets. We need to determine the temperature for each model facet, assuming it is a black body radiator, and calculate its thermal emission with the Planck function. The surface temperature is a result of several contributing energy transport processes within and outside of the asteroid, which are accounted for in the TPM. The Planck function is then integrated over all facets to obtain the total thermal emission of the asteroid. Finally, the predicted thermal output is fitted with observations.

The first TPMs for objects in space were developed for the Moon. These were able to reproduce thermal observations of the lunar surface, and also determine values for its thermal inertia and surface roughness which were matched by experiments on site by Apollo astronauts. The lunar surface models were generalized for spherical planetary bodies by Spencer et al. (1989) and Spencer (1990). The most used asteroid TPMs are all based on these two works. For a more detailed overview of the evolution of TPMs and references, see Delbo et al. (2015). The first TPM that accounts for eclipses and occultations in (doubly tidally locked) binary asteroid systems was reported by Mueller (2007). That model, referred to as binary TPM (BTPM), is used in this work.

In the rest of this section we will give an outline of the theory and implementation of TPMs in general as presented in Delbo et al. (2015), and of the BTPM as presented in Mueller (2007), see there for more details.

The BTPM starts with an energy balance at the asteroid surface. Incoming solar radiation heats the surface up. The intensity of the solar radiation I is inversely proportional to the distance r from the Sun squared. The energy coming onto the surface is proportional to the cosine of the angle between the Sun and the surface normal. A fraction A of the power in the total solar radiation on the asteroid surface will be scattered back. A is commonly known as the Bond albedo. The incoming solar radiation at the asteroid surface is then:

$$I = (1 - A)\frac{S_\odot}{r^2}\mu_S, \tag{2.1}$$

with $S_{\odot}$ the solar constant, which is the mean solar flux density at 1 AU from the Sun, and $\mu_S = \frac{\overrightarrow{r} \cdot \overrightarrow{n}}{r} = \cos(\theta)$, the cosine of the local solar zenith distance, which is defined to become 0 when the Sun is below the horizon. The surface may also be heated by secondary terms, such as scattered solar radiation, or reabsorbed thermal radiation within concave shapes. Since we assume a convex shape, we can neglect these secondary heating terms.

The absorbed solar energy can either be thermally re-emitted as a black body, or conducted down into the subsurface. The total power P emitted per unit area by an asteroid surface, assuming black body radiation, is given by the Stefan-Boltzmann law, which integrates the Planck radiation function over all frequencies and solid angles:

$$P = \epsilon \sigma T^4, \tag{2.2}$$

with T the surface temperature, σ the Stefan-Boltzmann constant, and ϵ the emissivity of the surface that gives the fraction of thermal power P that the asteroid can emit.

The heat flux Φ conducted down into the subsurface is proportional to the gradient of the temperature T. We will only consider heat transfer in the direction Z perpendicular to the surface, since the heat diffusion is only effective over a few centimeters and the model surface elements are much larger that that. Then:

$$\Phi = -\kappa \frac{\partial T}{\partial Z}, \tag{2.3}$$

with κ the thermal conductivity of the material.

Conservation of energy prescribes that the incoming energy should equal the outgoing energy at the surface:

$$\epsilon \sigma T^4 - \kappa \left(\frac{\partial T}{\partial Z} \right)_{Z=0} = (1-A) \frac{S}{r^2} \mu_S \tag{2.4}$$

The heat conduction is a diffusive process described by:

$$\rho C \frac{\partial T}{\partial t} = \frac{\partial}{\partial Z} \kappa \frac{\partial T}{\partial Z}, \tag{2.5}$$

where ρ is the surface mass density, and C is the specific heat capacity. The thermal conductivity κ is assumed to be independent of depth, and thus temperature. This assumption reduces the previous equation to the diffusion equation:

$$\frac{\partial T}{\partial t} = \frac{\kappa}{\rho C} \frac{\partial^2 T}{\partial Z^2} \tag{2.6}$$

Equation 2.6 is a second order differential equation, for which two boundary conditions are needed to be able to solve it. Equation 2.4 is the first boundary condition, for energy conservation at the surface. The second boundary condition is that the temperature should not change at infinite depth:

$$\left(\frac{\partial T}{\partial Z} \right)_{Z \to \infty} = 0 \tag{2.7}$$

The conservation of energy equation 2.4, diffusion equation 2.6 and infinite depth equation 2.7 give a complete coupled set of equations describing the thermal economy of the asteroid. To facilitate its computational solution it is preferable to cast the equations into a dimensionless form. To this end, we define the following dimensionless quantities, following Spencer et al. (1989):

$$\begin{aligned} \tau &= \omega t \\ z &= Z/l_s \\ u &= T/T_{SS} \end{aligned} \tag{2.8}$$

with angular frequency of the asteroid ω, and in which skin depth l_s, subsolar temperature T_{SS}, thermal parameter Θ and thermal inertia Γ are defined as:

$$\begin{aligned} l_s &= \sqrt{\frac{\kappa}{\omega\rho C}} \\ T_{SS} &= \sqrt[4]{\frac{(1-A)S_\odot/r^2}{\epsilon\sigma}} \\ \Theta &= \frac{\kappa/l_s}{\epsilon\sigma T_{SS}^3} = \sqrt{\omega}\frac{\Gamma}{\epsilon\sigma T_{SS}^3} \\ \Gamma &= \sqrt{\kappa\rho C} \end{aligned} \tag{2.9}$$

Thermal inertia is thus defined as a combined property of thermal conductivity, density and specific heat capacity.

This parametrization leads to the following coupled set of differential equations in terms of dimensionless quantities:

$$\frac{\partial}{\partial\tau}u(z,\tau) = \frac{\partial^2}{\partial z^2}u(z,\tau) \tag{2.10}$$

$$u(0,\tau)^4 = \mu_S(\tau) + \Theta\frac{\partial}{\partial z}u(0,\tau) \tag{2.11}$$

$$\lim_{z\to\infty}\frac{\partial}{\partial z}u(z,\tau) = 0. \tag{2.12}$$

This combination of equations depends only on the thermal parameter Θ, so this contains all the physics for the heat transfer mechanism. Θ is directly proportional to thermal inertia Γ and does not depend on any other thermal properties. However, κ, ρ and C cannot be determined separately with these equations, only the combined thermal inertia $\Gamma = \sqrt{\kappa\rho C}$. ρ and C are approximately constant for asteroid surfaces, but κ can vary over several orders of magnitude for different asteroids.

The source code of the BTPM is written in the C++ programming language. The program contains three main building blocks. Part I generates the shape of the asteroid system. Part II predicts lightcurves for the eclipses and occultations in the binary system. Finally, part III fits the grid of predicted lightcurves to the observed lightcurve.

Fixed asteroid parameters in the BTPM are the shape, spin period P, spin-axis orientation, absolute optical magnitude H and emissivity ϵ. Variable input parameters are thermal inertia Γ, beaming parameter η, area equivalent system diameter D and eclipse time offset Δt. The dimensionless factor η corrects for the effect of infrared beaming, which is the brightening of a rough surface at low observation phase angles. The rougher the surface, the larger this effect, so η is related to surface roughness. The area equivalent diameter D is related to geometric albedo p_V and the observed optical magnitude H. D is related to the diameters of the individual components D_1 and D_2 through $D^2 = D_1^2 + D_2^2$. The eclipse time prediction is uncertain within a few hours and the model finds the best fitting eclipse time offset Δt. The best fit of the observations with the model determines the best fit for D, Γ, η, Δt and the corresponding minimum χ^2.

The data flow in the three building blocks of the program is as follows:

- The starting point in part I is a predefined sphere. The main asteroid is an exact copy of this sphere. The accompanying asteroid is a rescale of this sphere, so that the ratio of both spheres represents the true mutual proportions of the asteroids. Then both asteroids are shifted in opposite directions along the X axis to scale with the actual distance between the two asteroids. The shift for each asteroid is inversely proportional to its mass, so that the system's center of mass lies in the origin. The two spheres are then saved as one system into a 3D graphics file.

- The second part of the program simulates the possible eclipses and occultations in the binary system. It takes the generated binary asteroid shape of the first part as input, along with the orbit and timing parameters. It also applies a grid of relevant physical properties, such as thermal inertia and roughness. A simulation over time then calculates the predicted lightcurves for the entire grid of variable parameters.

- The third part of the program fits the observed lightcurve to the grid of predicted lightcurves. This is implemented with a Monte Carlo simulation, which adds random noise to the observed lightcurves. This way the model determines the best fit including the error for the input physical properties. In particular, it determines a best fit thermal inertia for the given asteroid shape and eclipse event.

Details of the implementation can be found in Mueller (2007) and Mueller et al. (2010).

2.3 Physical interpretation of thermal inertia

The "looseness" of the surface material is an important factor in the total thermal inertia. A solid rock surface will react differently to temperature flux than a loose sandy surface. The solid rock will transfer heat more quickly to the inside and surface temperatures will not fluctuate easily, giving a high thermal inertia. In contrast, the sandy regolith will act as an insulator and not easily be penetrated by a heat wave. Thus heat remains on the surface and the surface quickly adapts its temperature, giving a low thermal inertia. This enables us to use thermal inertia as a **probe for the surface structure**.

See Figure 2.1 and 2.2 for illustrations of the thermal response for materials or objects with different thermal inertia. To get a feeling for values of thermal inertia for different materials and asteroids, Table 2.1 gives a few examples.

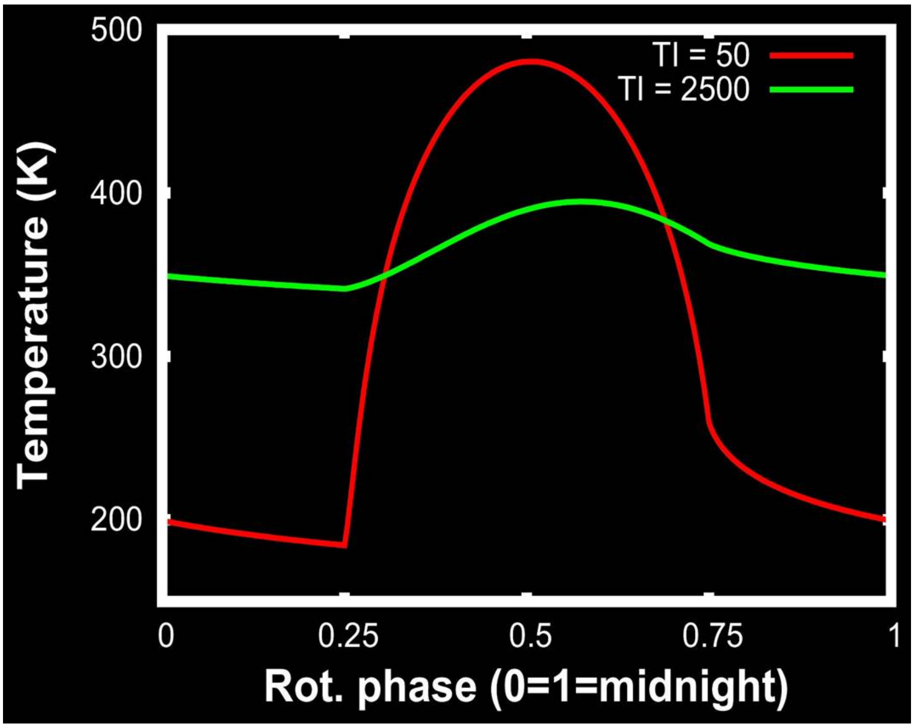

Figure 2.1: Response of two different materials to the daily temperature variation. Plotted is the temperature as a function of the day time. The red line shows the temperature variations for a low thermal inertia of TI = 50 J $s^{-1/2}$ K^{-1} m^{-2} (comparable with lunar regolith) and the green line for a high thermal inertia of TI = 2500 J $s^{-1/2}$ K^{-1} m^{-2} (comparable with bare rock). The higher the thermal inertia or resistance to surface temperature change, the less variation in surface temperature, and vice versa. Also note that the higher thermal inertia material stays warm inside for longer, so that the peak temperature is shifted to a later time than for the lower inertia material. Image credit: Migo Mueller.

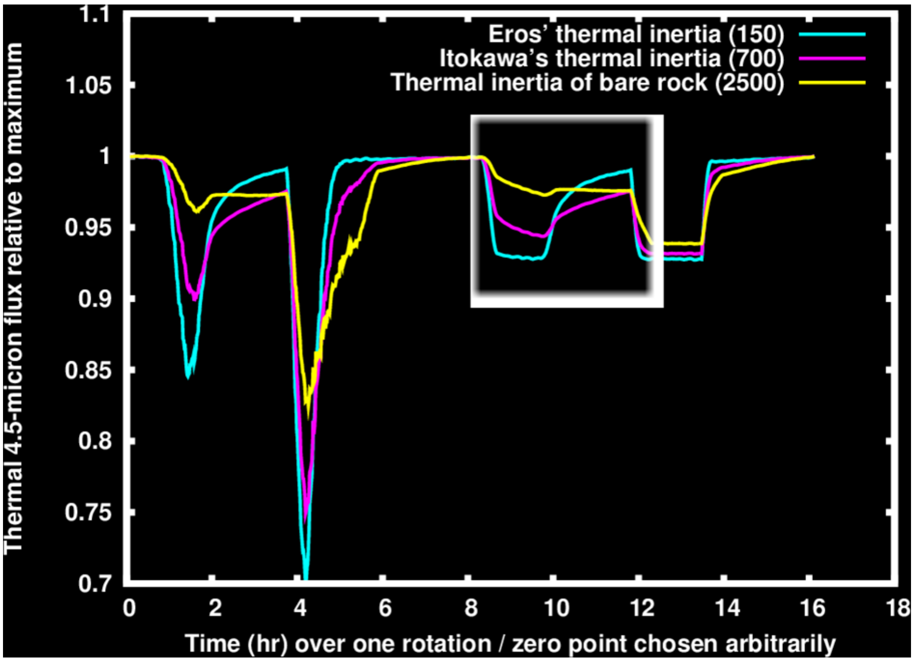

Figure 2.2: Model lightcurves of an eclipsing binary asteroid (not Patroclus!). Shown are lightcurves for three different thermal-inertia values (in J $s^{-1/2}$ K^{-1} m^{-2}). The white box contains the thermal response to a total eclipse event, where the larger component casts shadow on the smaller component. The remaining three events are irrelevant for the topic at hand. Low thermal inertia results in a large eclipse-induced flux drop, almost instantaneously at the start of the eclipse, and a quick heat-up after the eclipse. Higher thermal inertia reduces the drop amplitude and delays the response time. Image credit: Migo Mueller.

Material	κ (W $K^{-1}m^{-1}$)	ρ (kg m^{-3})	C (J $kg^{-1}K^{-1}$)	Γ (J $s^{-1/2}$ $K^{-1}m^{-2}$)
Nickel	91	8850	448	$19{\cdot}10^3$
Iron	81	7860	452	$17{\cdot}10^3$
Granite	2.9	2750	890	2600
Marble	2.8	2600	800	2400
Water ice, 0°	2.25	917	2000	2040
Water, 0°	0.56	1000	4200	1500
Snow (compact)	0.46	560	2100	740
Sandy soil	0.27	1650	800	600
Coal	0.26	1350	1260	665
Pumice	0.15	800	(900)	330
Paper	0.12	700	1200	320
Polystyrene foam	0.03	50	1500	47
Air	0.026	1.2	1000	5.6
Lunar regolith	0.0029	1400	640	51
Object	**Classification**	**R (AU)**	**D (km)**	**Γ (J $s^{-1/2}$ $K^{-1}m^{-2}$)**
1620 Geographos	NEA	1.1	5.04	340
1862 Apollo	NEA	1.0	1.55	140
1 Ceres	MBA	2.767	923	10
277 Elvira	MBA	2.6	38	250
2363 Cebriones	Trojan	5.2	82	7 ± 7
3063 Makhaon	Trojan	5.2	116	15 ± 15
Ganymede	Jupiter moon	5.2	5262	14 ± 2 (eclipse) $\sim$70 (diurnal)
Callisto	Jupiter moon	5.2	4820	11 ± 1 (eclipse) $\sim$50 (diurnal)
2060 Chiron	Centaur	13.6	166	4-5
10199 Chariklo	Centaur	15.8	302	1-16
50000 Quaoar	TNO	43	1082	6
90377 Sedna	TNO	87	995	0.1

Table 2.1: **Top** - Thermal properties of a selection of materials: thermal conductivity κ, mass density ρ, specific heat capacity C and thermal inertia Γ, all for temperatures of 20° unless otherwise stated. Values in parenthesis were estimated based on similar materials. Data as quoted after Mueller (2007), see there for original references. **Bottom** - Physical properties and thermal inertia of a selection of small bodies in the solar system: classification of type of object, semimajor axis of orbit around the Sun R, mean diameter D and thermal inertia Γ. The thermal inertia measuring method (eclipse/ diurnal) is specified when different methods were used. Data for the NEAs, MBAs, Trojans, Centaurs and TNOs as quoted after Delbo et al. (2015), thermal inertia for the Jupiter moons as quoted after Mueller et al. (2010), semimajor axes for the Trojans and Centaurs as quoted after IAU Minor Planet Center, diameters of Jupiter moons and Centaurs as quoted after JPL Small-Body Database Browser; see there for original references.

2.4 Yarkovsky effect

Thermal inertia not only controls the temperature distribution on the asteroid surface. It can also significantly alter the orbits of small asteroids via the Yarkovsky effect, named after its discoverer Ivan Osipovich Yarkovsky.

Consider a rotating object that is illuminated by the Sun. As illustrated in Figures 1.3 and 2.1, a higher thermal inertia will delay the maximum daily temperature. At the end of a day the surface temperature is higher than at the beginning of the day, because the heat has been absorbed by the subsurface and it takes time to cool down again. Consequently more photons are emitted on the evening side than on the morning side, resulting in a net force on the object that may significantly alter its orbit if it is not too large. See Figure 2.3 for an illustration of the Yarkovsky effect.

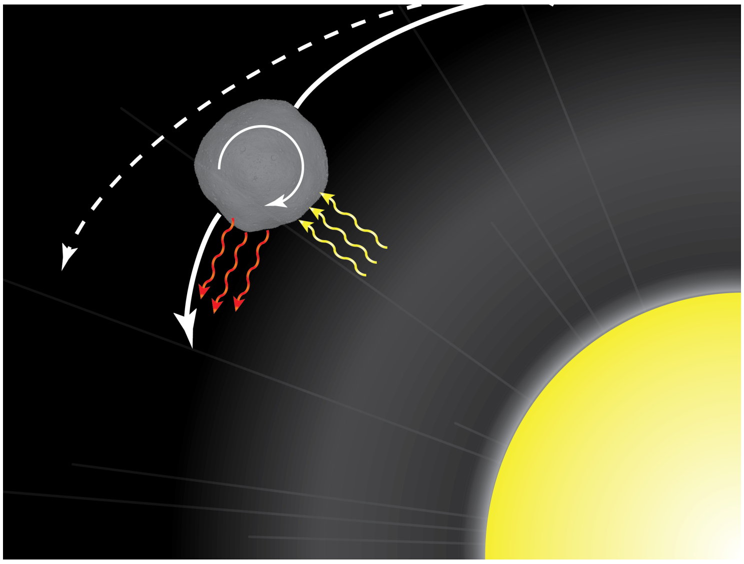

Figure 2.3: Illustration of the Yarkovsky effect. The Yarkovsky effect can push an asteroid closer to or farther away from the Sun. The asteroid is radiated by the Sun, the sunlight is indicated by yellow arrows. The depicted asteroid rotates retrograde and is warmer on the evening side. It thus effectively radiates more heat on the evening side than on the morning side. The excess photon emission is indicated by red arrows. The net recoil force on the asteroid is opposite the direction of its movement, causing it to slow down and spiral inward. If the asteroid is a prograde rotator, it radiates more heat on the other side, increasing the asteroid's speed and thus moving it outward. Figure from `https://dslauretta.com/2013/12/21/dewg-wheres-my-asteroid`.

This process can also cause an asteroid that was initially far from Earth to gradually come closer. The Yarkovsky effect is significant for asteroids smaller than 30 - 40 km in diameter (Vokrouhlický et al., 2015). Since collisions with Earth of even small asteroids are undesirable, it is worthwhile to investigate this process in more detail and systematically determine the thermal inertia of asteroids.

2.5 Asteroid spacecraft missions

Another practical reason for being interested in the thermal inertia of asteroids is that we would like to know its surface structure if we would want to land on it. Interest in asteroids as scientifically relevant objects and even as potentially containing mining resources are increasing so that this becomes a realistic scenario.

Not only that, Patroclus has been chosen as one of the targets of the Lucy mission, which is currently being developed by NASA. If approved, Lucy will fly by Patroclus in 2033, providing highly resolved data (see Figure 2.4). A fly by mission is a first step in spacecraft missions, then comes an orbiter mission and finally a lander mission.

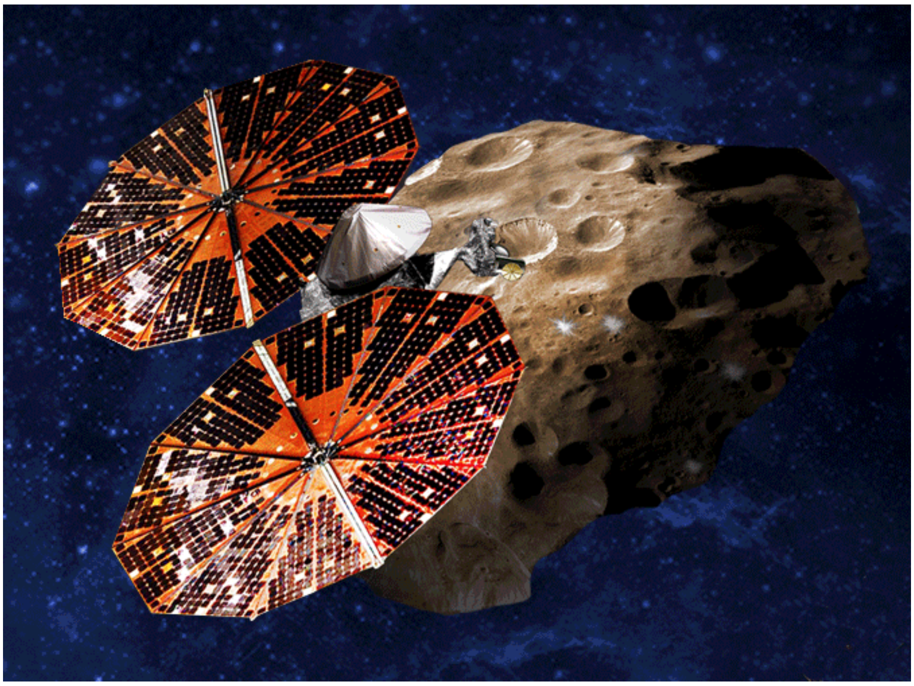

Figure 2.4: Artist impression of Lucy spacecraft targeting to visit six Jupiter Trojans including (617) Patroclus. Image credits: SwRI and SSL/Peter Rubin.

This may be far in the future for Patroclus, but asteroid lander missions are already a reality. At this moment, the Japanese JAXA's Hayabusa 2 and NASA's OSIRIS-REx spacecrafts are on the way to NEAs. Both will return samples from their target's asteroid surface back to Earth. The successful approach of the spacecrafts depends on accurate knowledge of surrounding temperatures, which are governed by thermal inertia. Both missions carry infrared spectrometers to obtain detailed in situ measurements of the thermal inertia to compare against remote-sensing results.

These missions follow up even earlier ones that have already visited several asteroids. NEAR Shoemaker visited (433) Eros in 2001 and Hayabusa visited (25143) Itokawa in

2005. Neither mission had a thermal instrument, but the thermal inertia measurements from earlier thermal studies are consistent with the expected thermal inertia based on the imagery of the spacecrafts (Mueller, 2007).

Also, the Rosetta space probe flew by (21) Lutetia in 2010 and did measure its thermal inertia (Capria et al., 2012; Schulz et al., 2012). These were in agreement with remote-sensing observations done from the ground and also with observations from the Spitzer Space Telescope and Herschel Space Observatory (Lamy et al., 2010; O'Rourke et al., 2012).

Chapter 3

Target & observations

We will first give some background information on our target asteroid, 617 Patroclus. Then we will describe the Spitzer observations of Patroclus by Mueller et al. (2010) that are the basis of this work. The new shape model by Buie et al. (2015), which ultimately triggered this research project, is described in Sect. 3.3.

3.1 617 Patroclus

617 Patroclus is one of the largest asteroids in the Trojan L_5 camp, named after the Greek warrior Patroclus. It was the second Trojan to be discovered, as early as 1906 by German astronomer August Kopff.

The spectral classification for Patroclus is P-type (Neese, 2010) (for the meaning of the asteroid spectral classifications see Sect. 1.3). It has a dark surface with a low geometric albedo of 0.0433 and its emissivity spectra reveal the presence of fine-grained($<$ few μm) silicates on the surface (Mueller et al., 2010).

It is not known where Patroclus was formed in the solar system. For a long time it was believed that the Trojans were formed near Jupiter (e.g. Marzari et al., 2002). But the Nice model by Morbidelli et al. (2005) shows that the Trojans might originate in the Kuiper belt. From there they may have been scattered over the solar system in a chaotic phase with resonant interactions of Jupiter and Saturn and ultimately have been captured in Jupiter's Lagrangian points. On the basis of their finding that Patroclus is mostly composed of water ice, Marchis et al. (2006) suggests that Patroclus could indeed be a former Kuiper belt object that has migrated inwards. However, Emery et al. (2011) hypothesize that of the two different compositional groups of Trojans (see Sect. 1.2), the less-red group originated near Jupiter or in the main asteroid belt. 617 Patroclus belongs to the less-red group of Trojans, which would mean it was formed nearby the present location in the middle of the solar nebula (Emery et al., 2015), contradicting the suggestion by Marchis et al. (2006).

Merline et al. (2001) discovered that Patroclus is a binary system, using adaptive optics to spatially resolve the system, see Figure 3.1. The main component remained Patroclus and its smaller companion was dubbed Menoetius.

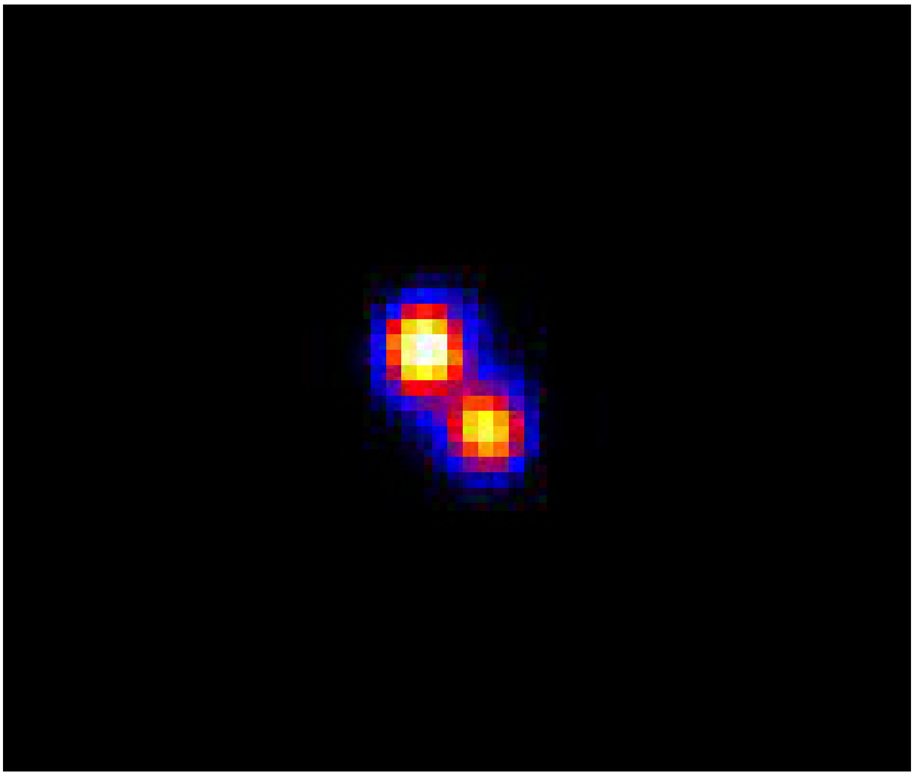

Figure 3.1: Patroclus and Menoetius, as viewed on October 13, 2001, from Gemini Telescope North, Mauna Kea, Hawaii (Merline et al., 2001).

If the components of a binary have different spin periods than the mutual orbit period, visible lightcurve observations will most likely show variations of multiple periodicity. Optical data of the Patroclus system obtained by Mueller et al. (2010) had low amplitude variations with only one single period. This indicates that both the primary and the secondary spin periods are fully synchronized to the mutual orbit period, so Patroclus and Menoetius are both tidally locked to each other. This means that the two components continuously face each other with the same side and the entire system can be treated as a rigid body. Such binaries are called *doubly synchronous binaries*.

The low amplitude of the lightcurve variations also indicated that both components are almost spherical, which motivated the initial assumption of a spherical shape by Mueller et al. (2010). The oblate Buie et al. (2015) model is however also consistent with this observation.

Marchis et al. (2006) obtained further spatially resolved observations of Patroclus, from which they derived the system's mutual orbit. They detected a near-infrared magnitude difference of 0.17 mag. Assuming similar albedo, the two companions are similar in size with the larger component being only ~ 1.082 times larger in diameter than the other. This was combined with thermal measurements for an estimate of the system size by Fernández et al. (2003) to give $D_1 = 121.8$ km and $D_2 = 112.6$ km.

They found the components to be separated by 680 $\pm$ 20 km and to go around each other in a period of 4.283 $\pm$ 0.004 days. This orbital information allowed them to determine the total system's mass at $1.36 \pm 0.11 \times 10^{18}$ kg. Together with the system size they obtained a low average mass density of $0.8^{+0.2}_{-0.1}$ g cm^{-3}. This suggests that both components are loose agglomerations of smaller clumps consisting mostly of water ice.

The Marchis et al. model was used to accurately predict the timing of a series of eclipse events in the Patroclus system in 2006-2007. It then reached one of its annual equinoxes, where the plane of the components' mutual orbits passes through the center of the Sun, so that the components regularly eclipse or occult each other. Several of these eclipse events have been observed in two separate campaigns by Berthier et al. (2007), and by Mueller et al. (2010).

Berthier et al. (2007) observed eclipse events with several ground-based telescopes. The new data allowed a further refinement of the Marchis et al. (2006) orbit model. They concluded that Patroclus and Menoetius orbit each other at a center-to-center distance of 654 $\pm$ 36 km and with a rotation period of 4.289 $\pm$ 0.05 days. Following Kepler's third law, the corresponding total system mass is $1.20 \pm 0.11 \times 10^{18}$ kg, and the corresponding diameters of Patroclus and Menoetius are 112 $\pm$ 16 km and 103 $\pm$ 15 km, respectively. The orbit is circular (eccentricity $\leqslant 0.001$) and features no precession.

Mueller et al. (2010) observed the thermal emission of the Patroclus system during two mutual eclipse events in June 2006. Those data are the basis of this work, see Sect. 3.2 for a description of the observations. Using a custom binary TPM (BTPM, see Sect. 2.2), they determined the thermal inertia of a Trojan asteroid for the first time. They obtained an average thermal inertia of 20 $\pm$ 15 J s$^{-1/2}$ K^{-1} m^{-2}. This indicates a top surface layer of loose small dust and soil pieces, which may vary over the surface. Furthermore, the model converged to component diameters of 106 $\pm$ 11 and 98 $\pm$ 10 km and a resulting average mass density of 1.08 ± 0.33 g cm^{-3}, overlapping within 1 σ with the values from Berthier.

3.2 Observations

Mueller et al. (2010) employed the InfraRed Spectrograph (IRS) (Houck et al., 2004) to observe the thermal emission of the Patroclus system during two eclipse events during June 2006. The IRS is one of the three science instruments on board the Spitzer Space Telescope (Werner et al., 2004). The observations were carried out in low-resolution spectroscopy mode, covering the infrared wavelength range 7.4 - 38 μm with resolution $R = \lambda/\mathrm{d}\lambda \sim 64$ - 128.

Two eclipse events were observed in June 2006. In event 1, Menoetius is shadowed by Patroclus and vice versa for event 2. Both events lasted about 4 hours and were observed from about 1-2 hours before the start of the eclipse, up to about an hour after the end of the eclipse. Spectra were obtained at 18 different times, 9 per event. Each observation had an integration time of approximately 6 minutes, which are snapshots compared to the total duration of the eclipse.

The start times of observations are given in Table 3.1. Observations 1.0 and 2.0

Observation	Day (June 2006)	Time (UT)	Observation	Day (June 2006)	Time (UT)
1.0	24	18:40	2.0	26	10:42
1.1	24	21:54	2.1	26	23:22
1.2	24	22:47	2.2	27	00:24
1.3	24	23:54	2.3	27	01:31
1.4	25	00:41	2.4	27	02:19
1.5	25	01:47	2.5	27	03:29
1.6	25	02:49	2.6	27	04:24
1.7	25	04:12	2.7	27	05:55
1.8	25	05:24	2.8	27	06:52

Table 3.1: Start times of the Spitzer observations during the two eclipses. There are 9 observations per event, labeled 1.0 - 1.8 for event 1 and 2.0 - 2.8 for event 2. Table copied from Mueller et al. (2010).

Event	1	2
Heliocentric distance r	5.947 AU	5.947 AU
Spitzer-centric distance Δ	5.95 AU	5.98 AU
Solar phase angle α	9.80°	9.77°
Heliocentric coordinates (J2000)	170.8°, +18.03°	170.9°, +18.00°
Spitzer-centric coordinates (J2000)	160.5°, +18.2°	160.7°, +18.1°

Table 3.2: Observing geometry of the eclipse events. The absolute visible magnitude for Patroclus equals $H = 8.19$, the slope parameter of the phase curve is assumed to be $G = 0.15$ (Tedesco et al., 2002). Table copied from Mueller et al. (2010).

were taken well before the start of the eclipses to enable comparison with the non-eclipse situation, and observations 1.7-1.8 and 2.7-2.8 were made to observe the warming up after the eclipse.

Figure 3.2 gives an impression of what the events will have looked like as seen from the Spitzer spacecraft. On the basis of this figure we roughly estimate that during maximum eclipse a fraction of ~ 40 % of the eclipsed asteroid is shadowed for event 1, and ~ 20 % for event 2.

Certain wavelength ranges were discarded from the analysis due to the presence of emissivity features (due to silicate grains), which are not accounted for in the BTPM. Each observation yielded usable data at 178 wavelengths, which adds up to 1602 data points per event of 9 observations. The observation geometry of the observations is summarized in Table 3.2.

The Spitzer observations have been reduced and calibrated by Mueller et al. (2010) to obtain the luminous flux during the eclipse happenings. The resulting fluxes can be found in data appendix A of their paper. These fluxes have been used in this research to fit the thermophysical model.

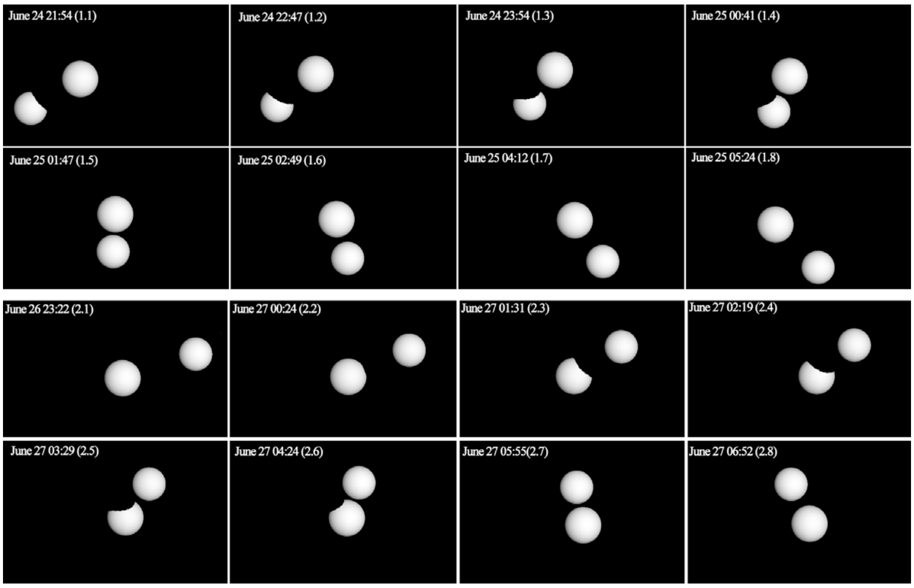

Figure 3.2: Impression of the two eclipse events, the labeling is the same as in Table 3.1. The top panel (1.1 to 1.8) is a reconstruction of the event 1 eclipse sequence on the basis of the corresponding Spitzer lightcurves. Bottom panel (2.1 to 2.8) repeats this for event 2. Figure copied from Mueller et al. (2010).

3.3 New shape model for Patroclus

Mueller et al. (2010) assumed a spherical shape for both components. But Buie et al. (2015) observed a stellar occultation by Patroclus and Menoetius and derived a more accurate shape. The tri-axial ellipsoid shape of (617) Patroclus that they determined sets the axial ratios of both components as $a : b : c = \mathbf{1.3 : 1.21 : 1}$, with mean-ellipsoidal axes of $127 \times 117 \times 98$ km for Patroclus and $117 \times 108 \times 90$ km for Menoetius. The uncertainty in these measurements is estimated to be about 3 km, with possible local deviations up to a scale of 5 km.

Patroclus and Menoetius are assumed to have their longest axis aligned with the direction towards each other. This is an expected configuration for two bodies that are tidally locked to each other. The tidal forces between their closest and farthest points from each other causes them to be stretched along their connecting line. The two bodies can then gradually lose their rotational energy to heat by the resulting internal friction and eventually become tidally locked with their longest axis pointing towards each other.

This new information on the shape and orientation is used in this research to refine the thermophysical model and determine the thermal inertia of the Patroclus system.

Chapter 4

Data analysis

Here we describe our reanalysis of the Spitzer observations of eclipses in the Patroclus system. As discussed above, Mueller et al. (2010) assumed spherical component shapes. We generalize this analysis by assuming ellipsoidal shapes including the one derived by Buie et al. (2015).

Firstly, we describe how we generate ellipsoidal binary shape models and how we visualize them. Sect. 4.2 forms the core of this section: we report the BTPM reanalysis of the eclipse data assuming first a spherical shape (to validate our numerical approach), then ellipsoidal shapes including the one derived by Buie et al.. Results are summarized in Sect. 4.2.3.

4.1 Asteroid models

We have made two adaptations to the code to create new asteroid shapes. First we have added a visualization method to enable a quick judgement by eye if the result is as expected. Second we have varied the parameters for the outer proportions to create asteroid shapes of different ellipticities.

4.1.1 Visualization

The code produces asteroid model files of a *.concave* format which lists all the vertices and facets as well as topological information that is used in the thermophysical model. This format is not easy to visualize. We have added an extra output file in *.obj* format that only lists the vertices and facets to enable visualization of the asteroid shape with easily available software.

The *.obj* format defines a 3D geometrical shape by digitizing its surface into separate facets. Each facet is defined by three or more points that are its corners or vertices. It is specified on one single line that starts with an 'f' and is followed by the identification numbers of its vertices (f v1 v2 v3). Each vertex is predined in the same file by listing its (x, y, z) coordinates on a single line that stars with a 'v' (v x y z). The *.obj* format

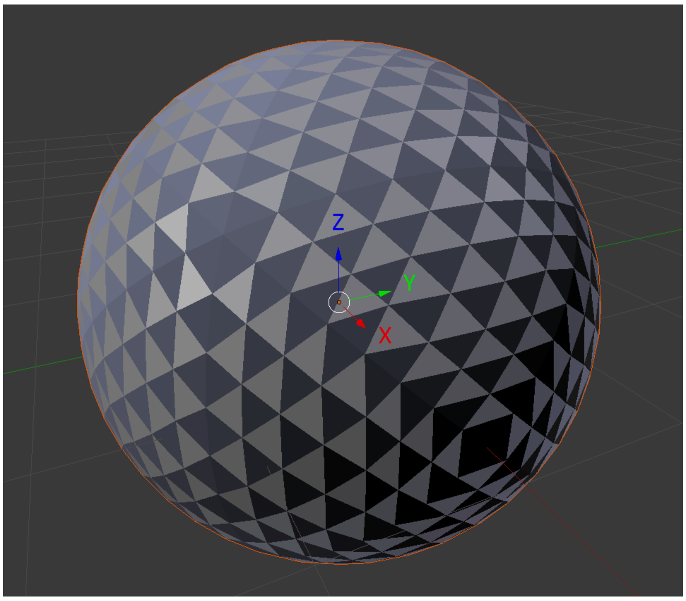

Figure 4.1: Geometric setup for the computational model of the asteroids. The image is a visualization in Blender of the original sphere from its *.obj* file (see text for explanation). This sphere is the starting point for the creation of new asteroid shapes, for example by stretching it into an ellipsoid.

also supports facets defined by more than three vertices, but we have used only triangular facets.

The *.concave* format already contains all the information that the *.obj* format requires. But it also includes additional information for the thermophysical model that makes it unreadable for *.obj* graphics programs. So we have written an extra function to create an *.obj* file that only contains the lines with facet identification numbers and vertex coordinates. This function had to account for the fact that *.obj* facets are one-based, so the first vertex is nr. 1. The *.concave* file is zero based, so the first vertex is nr. 0. The vertex numbers are therefore increased by 1 in the *.obj* format.

We used the open source 3D graphics software package Blender for the final visualization. See for example Figure 4.1 for the image of the predefined sphere that forms the starting point of the asteroid models.

At first glance this visualization seems exactly as expected. The sphere is formed by a surface of connected triangles and it seems to approach a spherical form as good as possible with this configuration. But a sphere can be rotated around any angle and map onto itself due to its circular symmetry. You would not notice any difference if the sphere was for example rotated around the X, Y or Z axis.

When we started to work with the elliptic asteroid models, we did notice a difference. As explained in Sect. 3.3, the longest axes of both asteroids should be aligned with the direction towards each other and they should be flattened in the plane of rotation, which is the XY plane. So the shortest axis should be in the Z direction. However, when we first looked at the elliptic asteroid models, the shortest axis was in the Y direction. At first sight, it seemed as if something was wrong with the model.

We then had a close look at the definitions of the axis orientations and recalculated some of the transformations between different coordinate systems. But these all seemed to be correct. Varying the axis ratios, eg. swapping the value for the b- and the c-axis, also gave the expected result. Then we looked at the *.obj* file itself and checked the maxima in the Y and Z coordinates, where the range in Y should be larger than in Z, given $a > b > c$. This was also correct. So a, b, c indeed seems to correspond to X, Y, Z, respectively. That led to the suspicion that the visualization in Blender might not be correct, so we looked at the asteroid models with two other 3D viewers. There the orientation was indeed correct, with the shortest axis along Z.

We finally found out that the problem is indeed a Blender specific issue. By default Blender assumes that objects in *.obj* files are projected with the Y axis upwards, but Blender always projects the Z axis upwards. This default orientation for *.obj* files is a remnant of 2D axis systems. For this reason Blender automatically rotates all imported *.obj* files 90 degrees along the X axis. (Explanation taken from blender.stackexchange.com.) We decided to still keep using Blender, since it is a versatile, flexible and easy to use software package. We thus apply a rotation of -90 degrees in X after importing any *.obj* file into Blender to obtain a correct physical visualization.

4.1.2 Creating new asteroid shapes

First, we verified whether we obtained the same binary shape model as Mueller et al. (2010) with two spherical components in part I of the thermophysical model (see Sect. 2.2). The code was not changed (apart from redefining system paths), but this does indicate if there are any system-dependent issues or compiler issues. We compared the two output *.concave* files with an automatic file differencing tool and found that the two files were identical. So the first part of the program had the expected output.

The tri-axial ellipsoid shape of 617 Patroclus as determined by Buie et al. (2015) sets the axial ratios of both components as $a : b : c = 1.3 : 1.21 : 1$. Our main goal is to determine the thermal inertia for this updated shape model. But to measure the sensitivity of the model to variations in the shape, we have also created several models in a range of axis ratios. The axis ratio that is used throughout this thesis to compare between different models is the ratio of the largest axis to the smallest axis a/c. The ratio of the intermediate axis to the smallest axis b/c is scaled proportional to the shape as observed by Buie et al..

By definition, the spherical model has axis ratio $a/c = 1$. The Buie shape model for Patroclus is our reference point with axis ratio $a/c = 1.3$, and accordingly $b/c = 1.21$.

For a gradual variation of shape models, we take the differences in sizes of the largest and intermediate axis between the sphere and the Buie model and multiply these differences by a fraction. The shape is then parametrized by the ellipticity fraction f_e:

$$\begin{aligned} a &= 1 + 0.3 f_e \\ b &= 1 + 0.21 f_e \\ c &= 1 \end{aligned} \tag{4.1}$$

Setting $f_e = 0$ creates a uniform sphere, and $f_e = 1$ will create the Buie shape model for Patroclus. This way we have created 7 different shape models in a grid of axis ratios a/c between 1 and 1.45 with steps of $f_e = 0.25$. We expect to find a good fit for or nearby the $a/c = 1.3$ model, given the accurate occultation observations by Buie et al. (2015).

The code had already defined the dimensions of the asteroids in the terms of the axial ratios $a : b : c$ of an ellipse. But all further calculations were initially performed for a sphere, not an ellipse. Now that we apply an elliptic model, we had to verify that all steps in the code were still valid for an ellipse as well.

In particular, the two volumes V_1 and V_2 of Patroclus and Menoetius are calculated in the code by a multiplication of all axial ratios with the volume equivalent diameter of each asteroid $D_{V,1}$ and $D_{V,2}$, respectively. The volume equivalent diameter of a shape is the diameter of a sphere with the same volume as the shape. The volume V_1 then becomes proportional to:

$$\begin{aligned} V_1 &\propto \frac{b_1}{a_1}\frac{c_1}{a_1} D_{V,1}^3; \\ &= \frac{b_1}{a_1}\frac{c_1}{a_1}\frac{a_1^3}{a_1^3} D_{V,1}^3; \\ &= a_1 b_1 c_1 \frac{D_{V,1}^3}{a_1^3}, \end{aligned} \tag{4.2}$$

and similarly for V_2 (taking out constant factors of $\frac{4}{3}\pi$ consistently). For a sphere, the fraction in the last equation becomes 1 and the volume is proportional to the radius to the third power, as expected. For an ellipse, the volume should be proportional to abc, so this last multiplication goes with a difference of a constant factor $(D_V/a)^3$. However, this is a constant throughout the model and does not influence the fit. Also the exact diameter is not used further in the code. So the code is still valid for an ellipsoid.

See Figure 4.2 for a visualization of the spherical and nominal ellipsoid asteroid shape model. This shows that the asteroids have the right shape and mutual proportions. We have verified that the most massive asteroid is closer to the center of mass, with the relative distances inversely proportional to their mass.

Given the observations by Buie et al. (2015), the actual shape of the asteroid system should closely resemble that of the bottom pair of ellipsoidal asteroids in Figure 4.2. Note that this shape represents the **new input in the TPM for this research**.

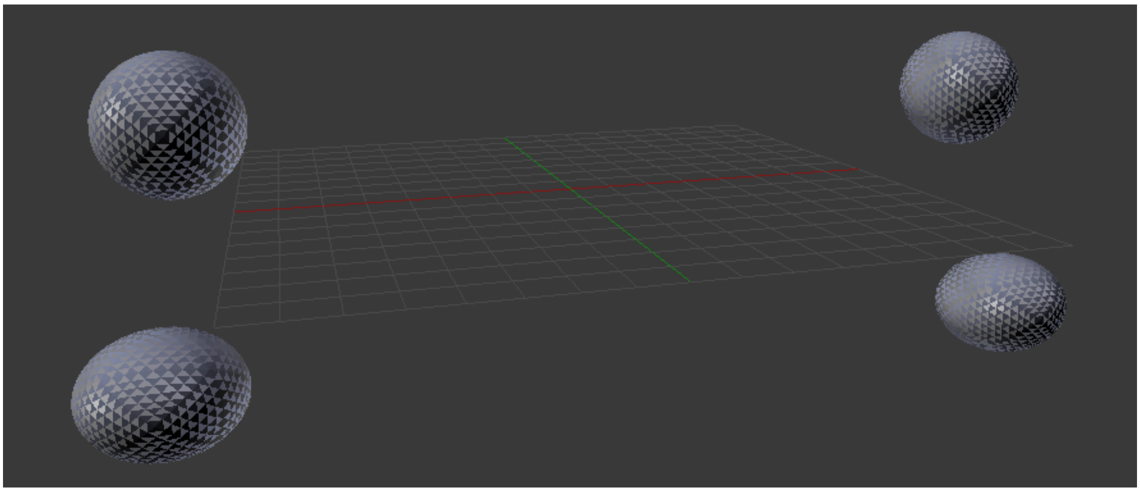

Figure 4.2: Visualization of two binary asteroid systems with different component shapes. The Z axis is upwards. The depicted plane is the XY plane, or plane of rotation. To distinguish the two systems, both have been translated in the Z direction, one upwards and one downwards. The models on top are spherical as in the first analysis by Mueller et al. (2010). The models on the bottom are elliptical with axial ratios of 1.3 : 1.21 : 1, which is the observed shape by Buie et al. (2015). In both cases, the larger Patroclus is on the left and Menoetius is on the right. Notice that Blender applies a perspective view, which seems to distort the alignment of the two asteroids. However, in 3D their longest axis are indeed aligned as required.

4.2 Fit model lightcurves to data

We continue the project with a validation of the results for a spherical model by Mueller et al. (2010) to make sure we run the thermophysical model properly and become familiar with its workings. We then proceed by implementing varying asteroid shapes for Patroclus and Menoetius, based on the observations by Buie et al. (2015). We conclude with the results of the BTPM for varying shapes.

4.2.1 Validation of analysis of spherical model

The analysis for each shape model is separated into four parts, for two eclipse events and two rotation axis positions for each eclipse event. In event 1, the larger Patroclus shadows the smaller Menoetius, and vice versa for event 2. The determination of thermal inertia is dominated by the thermal response of the shadowed component. Event 1 thus mostly represents the thermal inertia of Menoetius and event 2 mostly represents the thermal inertia of Patroclus. The axis positions refer to the orbit model rotation axis: the nominal one as given by Berthier et al. (2007) and an offset one probing the 1-σ uncertainty in axis (see Mueller et al., 2010, for details).

For each shape model, event and axis position the BTPM creates a grid of predicted

Parameter	Value	Reference
H	8.19 mag	Tedesco et al. (2002)
G	0.15	Tedesco et al. (2002)
ϵ	0.9	Hovis and Callahan (1966)
p_V	0.0433	Mueller et al. (2010)
P	4.289 days	Berthier et al. (2007)
R	654 km	Berthier et al. (2007)
D_1	113 km	Buie et al. (2015)
D_2	104 km	Buie et al. (2015)

Table 4.1: Input BTPM parameters for 617 Patroclus: absolute visible magnitude H, slope parameter G, emissivity ϵ, geometric albedo p_V, rotation period P, center-to-center distance R and component diameters D_1 and D_2. Following Kepler's third law for this binary system, the corresponding total system mass is 1.20×10^{18} kg. Model fluxes are calculated with the input geometric albedo and later rescaled to vary the diameters.

lightcurves for a range in thermal inertia Γ and beaming parameter η, which is specified by the user. The observed fluxes are then fitted to this grid of lightcurves. This gives the range in Γ and η for which a good fit can be found. In the final step, a best fit for Γ, η, diameter D and eclipse time offset Δt is determined.

Table 4.1 lists input parameters for the BTPM for Patroclus. For input parameters Γ and η we need to determine a proper range. The Monte Carlo simulation looks for a local minimum in χ^2. We require that the fitted parameter range falls well within the input parameter range. If the minimum χ^2 in a certain input parameter range is on the boundary of that range, the real minimum might be beyond that boundary. To have reasonable certainty that the local minimum is the global minimum, we require that the fit may not hit the boundaries of the input parameter range. Fitting the model in a wide grid of physical properties is computationally expensive. So we take a reasonably wide range and coarseness of the input grid.

For example, if the input thermal inertia values are between 3 and 6 J $s^{-1/2}$ K^{-1} m^{-2}, then the range for fitted thermal inertia should be between approximately 3.5 - 5.5 J $s^{-1/2}$ K^{-1} m^{-2} and the fit should never converge to the minimum or maximum input value. If the fit does contain either the minimum or maximum input value, the input parameter range is broadened until the fitting range falls well within it.

Since we had an expected outcome for the analysis of the spherical model, we chose a range of input parameters of Γ and η centered on those values. Then we calculated the BTPM through for the spherical model and for both events and both axis positions.

This revealed that some of the fits of the first results by Mueller et al. (2010) did occasionally hit the boundaries of the input grid of physical properties. The boundaries of the grids therefore had to be widened. However, this hardly changed the final best fit parameters.

Tables 4.2 and 4.3 compare the results by Mueller et al. (2010), with our validation of this result, respectively. The values per event are clearly strongly overlapping and almost

	χ^2	Γ (J s$^{-1/2}$ K^{-1} m^{-2})	η	D (km)
Event 1	2543 ± 84	20.7 ± 3.8	0.762 ± 0.014	145.7 ± 0.3
	2586 ± 84	7.6 ± 1.7	0.814 ± 0.008	146.0 ± 0.3
Event 2	3566 ± 102	6.4 ± 0.9	0.838 ± 0.005	143.4 ± 0.3
	3847 ± 109	5.1 ± 0.8	0.845 ± 0.004	143.1 ± 0.3

Table 4.2: Output BTPM parameters for the best fit by Mueller et al. (2010) for events 1 and 2 in the case of a spherical asteroid model. For each event the model is calculated for a nominal solution of the orbit model in the top line and an offset solution of 1σ in the bottom line. Listed parameters are minimum χ^2, thermal inertia Γ, beaming parameter η and area equivalent diameter D. There are 1602 data points per event, so the reduced χ^2 is in the order of 1.6 to 2.4.

	χ^2	Γ (J s$^{-1/2}$ K^{-1} m^{-2})	η	D (km)
Event 1	2541 ± 84	20.7 ± 3.9	0.762 ± 0.013	145.7 ± 0.3
	2588 ± 84	7.7 ± 1.8	0.814 ± 0.008	146.0 ± 0.2
Event 2	3566 ± 106	6.4 ± 1.2	0.838 ± 0.006	144.8 ± 0.2
	3845 ± 111	5.2 ± 0.7	0.845 ± 0.004	144.5 ± 0.2

Table 4.3: Output BTPM parameters for the best fit in our rerun of the thermophysical model in the case of a spherical asteroid model, to be compared with Table 4.2.

all of them are within each other's error bounds. The values do not have to be exactly the same to validate the result of the first research, since the fitting procedure applies a Monte Carlo simulation with random Gaussian noise added to the data. Small variations are therefore expected.

Two of our results are significantly different from those given in Mueller et al. (2010): the diameters for event 2. As confirmed by M. Mueller, this is due to an oversight in the preparation of their manuscript. Final results were inadvertently generated using different code versions, which differed in the application of a diameter correction factor. Our diameter results for event 2 are therefore an improvement over those presented by Mueller et al., although the ~ 1 % improvement is small compared to the systematic diameter uncertainty of ~ 10 %.

To make the determination of the boundaries for the input parameter range easier for the remainder of the project, we have added functions in part III of the model to output the minimum and maximum of the fit and compare this with the input values. It is then easily seen whether the range of input values should be widened.

4.2.2 Run model with new asteroid shapes

Now we turn to the analysis of the BTPM for varying ellipsoidal shapes. The basic input parameters are the same as in Table 4.1. The nominal shape is the new shape for Patroclus as determined by Buie et al. (2015) with $a : b : c = 1.3 : 1.21 : 1$. We vary shapes by varying a/c, and scaling b/c proportional to the nominal shape, as explained in Sect. 4.1.2. This way we create a spectrum of seven different shapes, from a sphere to an even more ellipsoidal shape than the Buie model.

The code needed adjustments to accommodate the different shape models. The data structure was changed so that the output for different shape models is saved in separate folders for each model. The files with the final fits also received an additional suffix for a clear distinction between different events and different axis positions for different shapes.

The first step was to implement the new shapes in part I of the model by applying the new axis ratios. We verified that all new shapes looked as expected, by inspecting the gradual increase in axis ratios with more and more ellipsoid models, and checking the orientation of the rotation axis.

We then determined the input range in Γ and η for which the BTPM finds best fits, again with the requirement that all fitted values fall well within the considered input range. For each new model we used the input parameters for Γ and η of the previously fitted model as the starting point, assuming that a small change in the shape will not drastically change the eclipse event. So for the $a/c = 1.075$ model we started with the fitted parameter range from the $a/c = 1$ model, and so on. Since the data volume in model lightcurves significantly increases with a larger range of input parameters, we start with a coarse grid for each shape model of $[\Delta\Gamma = 2, \Delta\eta = 2]$.

We then run the full BTPM over this range of input parameters. Whenever a fit converged to one of the boundaries of this range, the boundaries were expanded until none of the fits hit any of the input boundaries. This way we determined a coarse range of proper input values of Γ and η for each shape, event and axis position.

The model grids were then further refined to $[\Delta\Gamma = 0.25, \Delta\eta = 0.25]$ to obtain a fine grid of lightcurves for all combinations of the considered values of Γ and η. The code checks whether a lightcurve is already calculated for a certain Γ and η and skips these values if the file with the lightcurve already exists. We thus constantly refined the grids in factors of two, so that previous results could be reused in the new calculations. In the case of the three most elliptical models the thermal inertia reached low values to nearly 0, so in those cases the grid for thermal inertia was even further refined by a factor two.

Finally, we determined the best fit for each shape, eclipse event and axis position. The output of the third program part of the BTPM is a file with the best fit values for each of the 5000 lightcurves with random noise that are created in the Monte Carlo simulation. The best fit over all these values is determined with a separate IDL routine (which was already available).

We report the applied input ranges and the corresponding best fits for Γ and η in Table 4.4.

Event	Axis	$[\Gamma_{min}, \Gamma_{max}]$ ($\mathrm{Js^{-1/2}K^{-1}m^{-2}}$)	Best fit Γ ($\mathrm{Js^{-1/2}K^{-1}m^{-2}}$)	$[\eta_{min}, \eta_{max}]$	Best fit η
$a/c = 1$					
1	Nominal	10.50 – 34.00	20.7 ± 3.85	0.7200 – 0.8000	0.762 ± 0.013
	Off	0.00 – 16.75	7.69 ± 1.82	0.7775 – 0.8525	0.814 ± 0.008
2	Nominal	3.50 – 15.00	6.41 ± 1.16	0.8000 – 0.8525	0.838 ± 0.006
	Off	2.75 – 8.00	5.15 ± 0.75	0.8300 – 0.8575	0.845 ± 0.004
$a/c = 1.075$					
1	Nominal	4.25 – 29.25	15.8 ± 2.65	0.7250 – 0.8175	0.770 ± 0.010
	Off	0.00 – 15.00	4.37 ± 1.69	0.7750 – 0.8425	0.819 ± 0.008
2	Nominal	2.25 – 13.75	5.55 ± 2.57	0.7975 – 0.8500	0.833 ± 0.012
	Off	2.25 – 6.25	3.81 ± 0.60	0.8300 – 0.8525	0.841 ± 0.003
$a/c = 1.15$					
1	Nominal	0.00 – 8.75	3.49 ± 1.48	0.7875 – 0.8325	0.813 ± 0.007
	Off	0.00 – 2.50	0.25 ± 0.26	0.8175 – 0.8375	0.830 ± 0.002
2	Nominal	1.25 – 5.25	2.58 ± 0.52	0.8250 – 0.8475	0.838 ± 0.003
	Off	1.00 – 3.00	1.78 ± 0.31	0.8325 – 0.8500	0.843 ± 0.002
$a/c = 1.225$					
1	Nominal	0.00 – 2.50	0.16 ± 0.28	0.8075 – 0.8275	0.820 ± 0.002
	Off	0.00 – 1.75	0.45 ± 0.39	0.8100 – 0.8250	0.818 ± 0.003
2	Nominal	0.75 – 3.50	1.82 ± 0.44	0.8225 – 0.8425	0.833 ± 0.003
	Off	0.25 – 2.25	0.63 ± 0.29	0.8300 – 0.8475	0.839 ± 0.002
$a/c = 1.3$					
1	Nominal	0.000 – 1.000	0.209 ± 0.164	0.8050 – 0.8175	0.811 ± 0.002
	Off	0.000 – 0.875	0.252 ± 0.149	0.8025 – 0.8150	0.809 ± 0.002
2	Nominal	0.375 – 2.250	1.115 ± 0.336	0.8200 – 0.8350	0.828 ± 0.002
	Off	0.250 – 1.250	0.690 ± 0.150	0.8225 – 0.8375	0.830 ± 0.002
$a/c = 1.375$					
1	Nominal	0.000 – 0.625	0.110 ± 0.107	0.7975 – 0.8075	0.802 ± 0.002
	Off	0.000 – 0.375	0.060 ± 0.079	0.7950 – 0.8075	0.801 ± 0.002
2	Nominal	0.375 – 1.625	0.771 ± 0.178	0.8150 – 0.8275	0.821 ± 0.002
	Off	0.125 – 1.125	0.542 ± 0.151	0.8150 – 0.8275	0.822 ± 0.002
$a/c = 1.45$					
1	Nominal	0.000 – 0.250	0.015 ± 0.059	0.7875 – 0.7975	0.793 ± 0.002
	Off	0.000 – 0.125	0.000 ± 0.000	0.7875 – 0.7975	0.793 ± 0.002
2	Nominal	0.000 – 1.125	0.425 ± 0.160	0.8075 – 0.8200	0.814 ± 0.002
	Off	0.000 – 0.750	0.261 ± 0.170	0.8075 – 0.8200	0.814 ± 0.002

Table 4.4: Results of the thermophysical model for shape models $a/c = 1$ to 1.45. The analysis for each shape model is separated into four parts: for two eclipse events and two axis positions for each eclipse event. Tabulated are the fitted range and the best fit for Γ, and the fitted range and best fit for η.

4.2.3 Results

Figures 4.3 to 4.6 plot the results for the seven different shape models, two events and two axis positions. We distinguish in particular between event 1 and 2 in the results, given that they are two separate happenings and may also indicate different physical properties between Patroclus and Menoetius.

Figure 4.3 plots the best fit thermal inertia Γ as function of shape. This figure represents the main result of this research. The shape is expressed in terms of axis ratio a/c, with a the longest axis and c the shortest axis of the asteroid. The new shape model for Patroclus corresponding to the observations by Buie et al. (2015) has axis ratio $a/c = 1.3$. For the numerical values of the plotted quantities we refer to the fourth column with the best fit for Γ in Table 4.4.

In the plot, we show four lines. The red and green lines represent the nominal axis and off axis configuration of event 1, respectively. The blue and black lines represent the nominal axis and off axis configuration of event 2, respectively. The error bars have been obtained by a Monte Carlo evaluation of the uncertainties in the observations. The thermal inertia varies between 0.0 to 20.7 J $s^{-1/2}$ K^{-1} m^{-2} (also see the fourth column in Table 4.4). In all cases we see a clear general downward trend of thermal inertia as the asteroid becomes more elongated.

Note the substantial difference between the red and green line of event 1 for low axis ratios, specifically in the range of $a/c \approx 1.0 - 1.15$. In other words, the thermal inertia is considerably different towards a more spherical shape between the nominal and off axis case of event 1. In varying the shape from $a/c = 1$ to 1.15 the thermal inertia plummets to only 17 % of its value in the nominal axis case. Over this range the value for thermal inertia for the nominal axis is 2-3 times higher than for the off axis. From Table 4.4 we read for event 1 that at the nominal value of $a/c = 1.3$, $\Gamma = 0.209 \pm 0.164$ J $s^{-1/2}$ K^{-1} m^{-2} for the nominal axis and $\Gamma = 0.252 \pm 0.149$ J $s^{-1/2}$ K^{-1} m^{-2} for the off axis.

For event 2, we see that the black and blue line overlap within 1 σ. Over the entire range of explored axis ratios the nominal axis model (blue) attains a higher thermal inertia than that of the off axis model (black). From Table 4.4 we read for event 2 that at the nominal value of $a/c = 1.3$, $\Gamma = 1.115 \pm 0.0.336$ J $s^{-1/2}$ K^{-1} m^{-2} for the nominal axis and $\Gamma = 0.690 \pm 0.150$ J $s^{-1/2}$ K^{-1} m^{-2} for the off axis.

For low axis ratios from $a/c = 1$ to 1.075, event 1 has a higher thermal inertia than event 2, with a factor of 2-3. Interestingly, for axis ratios from $a/c = 1.225$ and higher, we find that the thermal inertia of event 2 becomes higher than for event 1, in the order of a factor 3 to 4 for $a/c = 1.3$ and even higher at higher axis ratios.

Figure 4.4 plots the best fit for the beaming parameter η as a function of varying shape. This is a dimensionless factor with which the flux is corrected for the infrared beaming effect and which is related to surface roughness (see Mueller, 2007). The lines and error bars have the same meaning as in Figure 4.3. The value for η ranges from 0.76 to 0.84 over all cases. For the numerical values of the plotted quantities we refer to the sixth column with the best fit for η in Table 4.4.

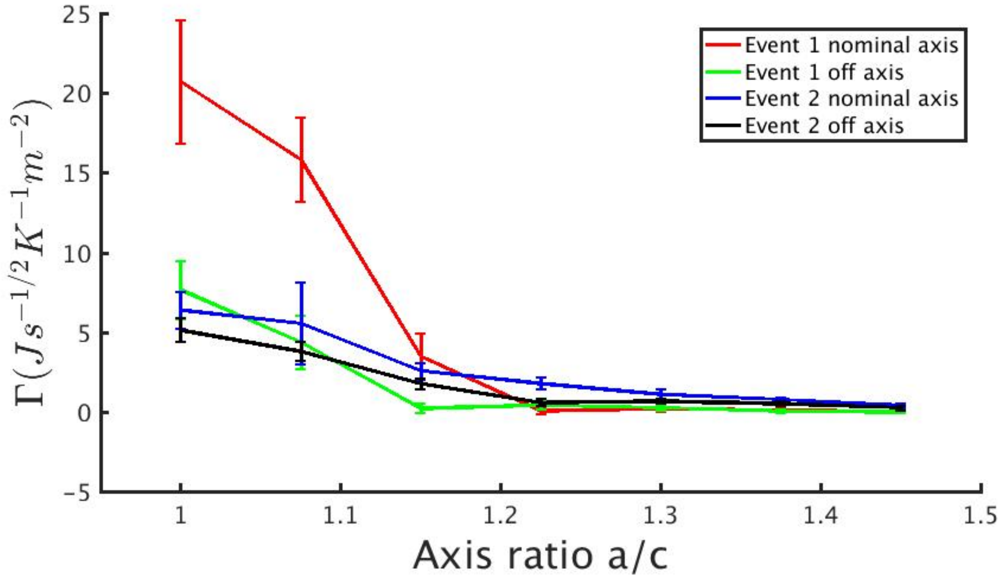

Figure 4.3: Thermal inertia as a function of shape. Plotted are the best fit thermal inertia values as a function of axis ratio a/c. This figure represents the main result of this research.

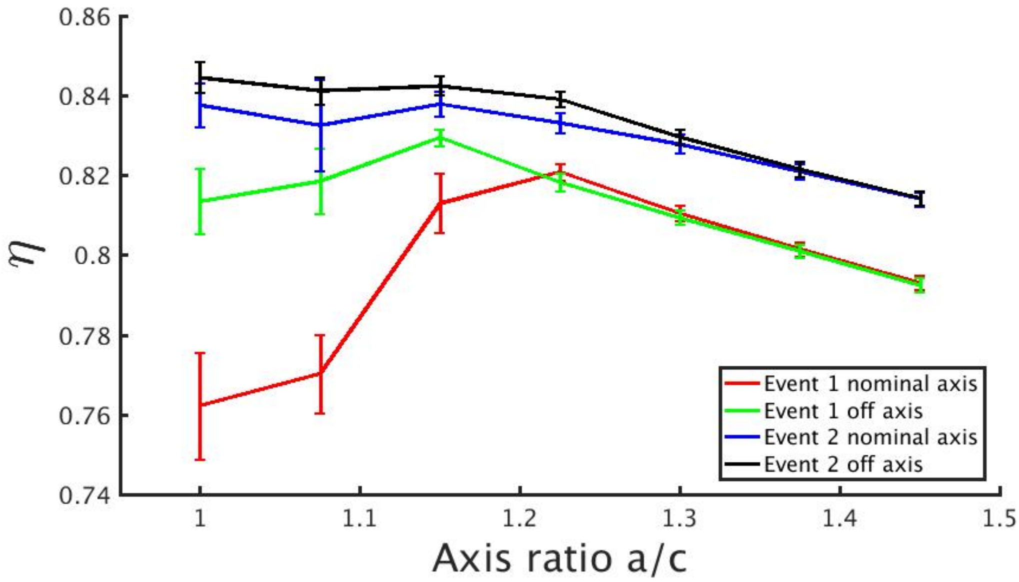

Figure 4.4: Beaming parameter η as a function of shape. The plot shows the best fit η parameter as a function of axis ratio a/c.

For event 2, we see a gradual downward trend in η for $a/c > 1.15$, following a plateau for lower axis ratios. The value of η for the off axis case of event 2 is for all shapes $\geqslant \eta$ of the nominal axis case. The difference in η between the nominal and off axis case of event 2 is the highest for $a/c = 1.075$, with $\Delta\eta = 0.008$. From Table 4.4 we read for event 2 that at the nominal value of $a/c = 1.3$, $\eta = 0.828 \pm 0.002$ for the nominal axis and $\eta = 0.830 \pm 0.002$ for the off axis.

Event 1 displays a more complex behavior than event 2. While it has the same downward trend for high axis ratios, it shows an increasing trend for lower axis ratios, with a turnaround point at $a/c > 1.15 - 1.225$. For lower axis ratios than $a/c = 1.225$ the nominal axis model has substantially lower values of η than the off axis models (and the values for event 2), up to a difference in η of 0.05. For higher axis ratios the nominal and off axis values in event 1 for η are almost equal. From Table 4.4 we read for event 1 that at the nominal value of $a/c = 1.3$, $\eta = 0.811 \pm 0.002$ for the nominal axis and $\eta = 0.809 \pm 0.002$ for the off axis.

Comparing event 1 with event 2, we note that over the entire range of shape models the values for η of event 2 are higher than for event 1. The maximum difference in η between event 1 and 2 is 0.076 for the spherical model. Towards higher axis ratios, the difference in η between event 1 and 2 becomes an approximately constant 0.021.

Figure 4.5 shows a general monotonous increase of area equivalent diameter D with increasing asteroid axis ratio. The variation in diameter is not large, smaller than 10 %. This is still smaller than the maximum systematic uncertainty in diameter of 10 %, estimated from maximum systematic uncertainties in TPM-derived diameters in the case of near-Earth asteroids (see Mueller et al., 2010).

For event 1, the two shape models with the lowest axis ratio have a smaller D for the nominal axis model than the off axis model, and vice versa for higher axis ratios. At the nominal value of $a/c = 1.3$, $D = 154.7 \pm 0.2$ km for the nominal axis and $D = 154.2 \pm 0.2$ km for the off axis. For event 2, all shape models have a smaller D for the off axis model than for the nominal axis model. At the nominal value of $a/c = 1.3$, $D = 152.7 \pm 0.2$ km for the nominal axis and $D = 152.1 \pm 0.2$ km for the off axis.

Comparing event 1 with event 2, for all shape models event 1 uniformly has a larger area equivalent diameter than event 2 of ~ 1 %.

Figure 4.6 plots the minimum χ^2 per shape model. We see a clear difference between event 1 and 2. The minimum χ^2 is invariably lower for event 1 than for event 2 by a factor of 25 to 50 %.

For event 1, the minimum χ^2 is found for axis ratios a/c of 1 - 1.075. The nominal axis solution has a lower χ^2 for all shape models by a factor of around 2 - 8 %. At the nominal value of $a/c = 1.3$, $\chi^2 = 2936 \pm 91$ for the nominal axis (reduced $\chi^2 = 1.85 \pm 0.06$) and $\chi^2 = 3155 \pm 97$ for the off axis (reduced $\chi^2 = 1.99 \pm 0.06$).

The minimum χ^2 with the best fit for event 2 is found around axis ratios a/c of 1.075 - 1.15. The nominal axis solution has a lower χ^2 for all shape models by a factor of around 5 - 10 %. At the nominal value of $a/c = 1.3$, $\chi^2 = 3542 \pm 104$ for the nominal axis (reduced $\chi^2 = 2.22 \pm 0.07$) and $\chi^2 = 3966 \pm 112$ for the off axis (reduced $\chi^2 = 2.50 \pm 0.07$).

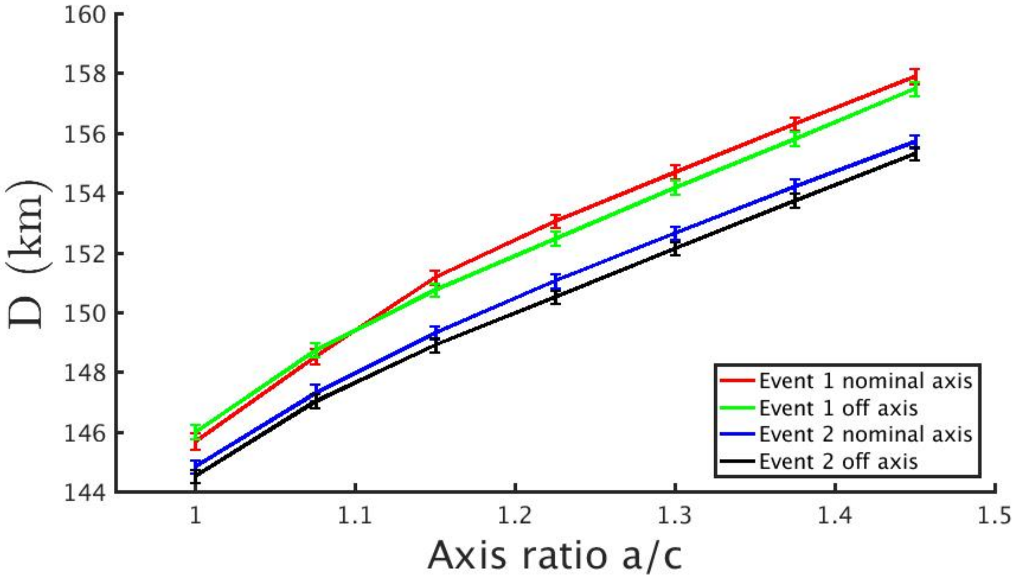

Figure 4.5: Diameter as a function of shape. Plotted is the best fit area equivalent diameter as a function of axis ratio a/c.

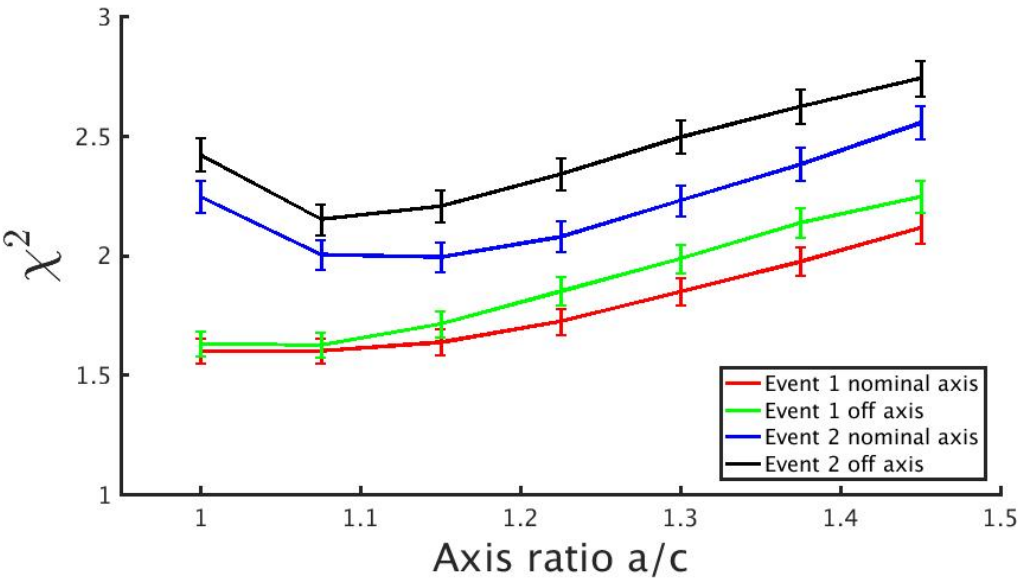

Figure 4.6: Reduced χ^2 of the BTPM fits as a function of shape. Plotted is the best fit reduced χ^2 as a function of axis ratio a/c.

	χ^2	Γ (J s$^{-1/2}$ K^{-1} m^{-2})	η	D (km)
Event 1	2936 ± 91	0.209 ± 0.164	0.811 ± 0.002	154.7 ± 0.2
	3155 ± 97	0.252 ± 0.149	0.809 ± 0.002	154.2 ± 0.2
Event 2	3542 ± 104	1.115 ± 0.336	0.828 ± 0.002	152.7 ± 0.2
	3966 ± 112	0.690 ± 0.150	0.830 ± 0.002	152.1 ± 0.2

Table 4.5: BTPM parameters for the best fit for ellipsoidal components with axial ratios of 1.3 : 1.21 : 1. (This corresponds to the Buie model for Patroclus and Menoetius.) For each event the model is calculated for a nominal solution of the orbit model in the top line and an offset solution of 1σ in the bottom line. Listed parameters are minimum χ^2, thermal inertia Γ, beaming parameter η and area equivalent diameter D.

	Event 1	Event 2
D	154 ± 15 km	152 ± 15 km
D_1	113 ± 11 km	112 ± 11 km
D_2	105 ± 10 km	103 ± 10 km
ρ	0.88 ± 0.26 g cm^{-3}	0.92 ± 0.26 g cm^{-3}
Γ	0.23 ± 0.17 J s$^{-1/2}$ K^{-1} m^{-2}	1.0 ± 0.45 J s$^{-1/2}$ K^{-1} m^{-2}
η	0.810 ± 0.003	0.829 ± 0.003

Table 4.6: Best fit parameters for event 1 & 2 with the Buie model, following from Table 4.5: area equivalent diameter D, individual asteroid diameters D_1 and D_2, mean density ρ, thermal inertia Γ and beaming parameter η. This is the nominal solution for the new shape model by Buie et al. (2015) of Patroclus.

Table 4.5 shows the outcome for χ^2, Γ, η and D in the case of two ellipsoidal components of Patroclus with axial ratios of 1.3 : 1.21 : 1, as in the shape model observed by Buie et al. (2015). Table 4.6 specifies the corresponding best fit parameters per event 1 and 2, including the resulting individual asteroid diameters and average system density. For the diameter a conservative upper limit on the systematic uncertainty of 10 % is assumed. These best fit parameters are the nominal solution for the new shape model for Patroclus.

As Figure 4.3 shows, the determination of thermal inertia is strongly dependent on uncertainties in the shape model. Following the varied shape TPM by Hanuš et al. (2015) we have investigated the behavior of χ^2 as a function of thermal inertia for the different shapes. The results are plotted in Figures 4.7 and 4.8 for event 1 and 2, respectively. Each data point in these plots represents the best fit for thermal inertia for each shape model. We have tried to identify the optimal fit for thermal inertia for each event over all shapes.

For event 1, we should note that the range in thermal inertia for the green line, i.e. the off axis model, is considerably shorter than that for the nominal model represented in the red line (also cf. Figure 4.3). In the plot we included an insert that zooms in on low Γ values.

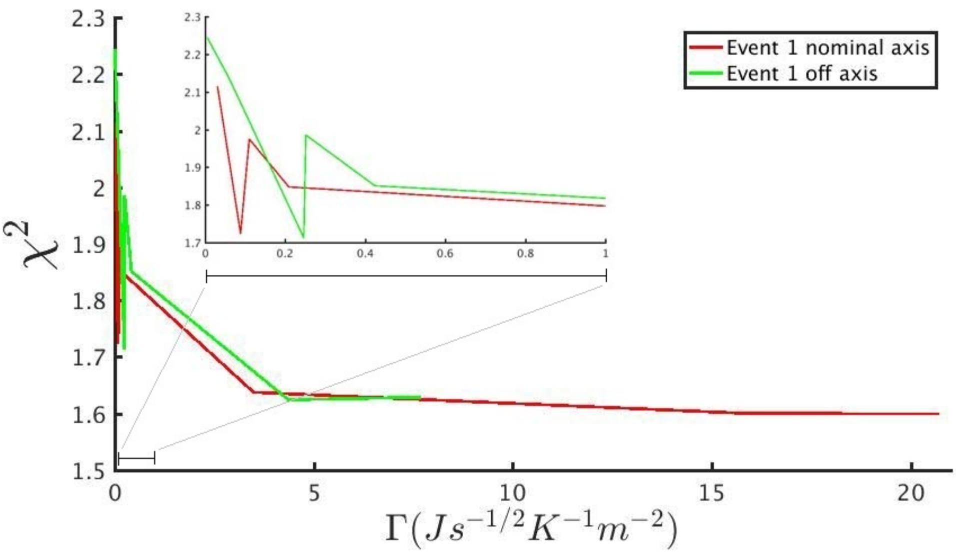

Figure 4.7: Reduced χ^2 as a function of thermal inertia for event 1. The insert diagram zooms in on the lowest values of thermal inertia. Each data point represents the minimum χ^2 for a specific shape model. There is no clear minimum for χ^2. Only for the off axis solution a faint minimum may be indicated. To extrapolate the data more to the right of this graph, the normally longest axis of the asteroid would become the shortest, which is highly unlikely for Patroclus.

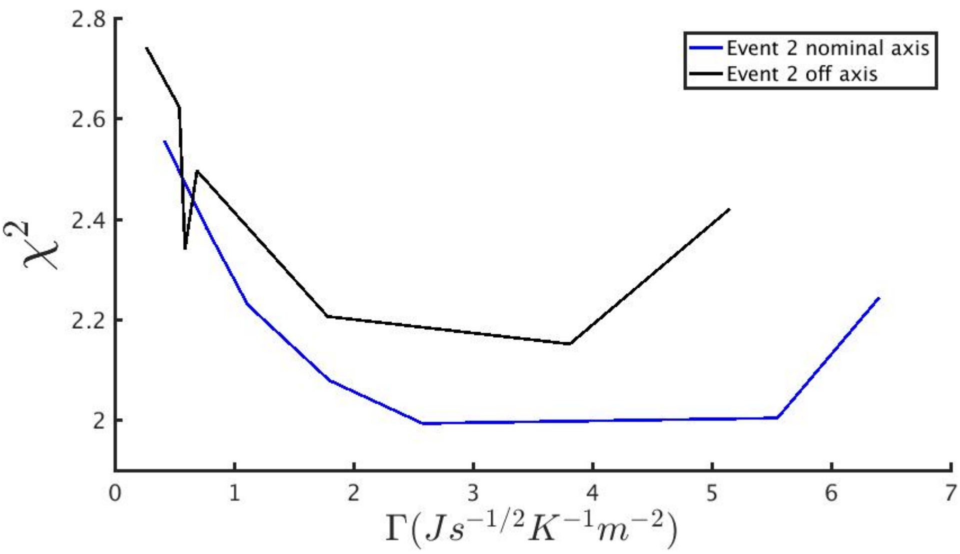

Figure 4.8: Reduced χ^2 as a function of thermal inertia for event 2. Each data point represents the minimum χ^2 for a specific shape model. The best fit for thermal inertia lies at the minimum for χ^2. We estimate this to be 4 $\pm$ 2 J $s^{-1/2}$ K^{-1} m^{-2} for the nominal axis and 3 $\pm$ 2 J $s^{-1/2}$ K^{-1} m^{-2} for the off axis solution.

The χ^2 distribution for the thermal inertia has a broad base for event 1. Given that χ^2 does not show a clear minimum for the current data, an outstanding signal cannot be immediately detected. However, there is a faint indication for a minimum in a range of 4-8 J $s^{-1/2}$ K^{-1} m^{-2} for the off axis solution of event 1. For $\Gamma > 1$ the two lines for the nominal and off axis are similar within ~ 3 %. For $\Gamma < 1$ we observe fluctuations. This seems to be related to the small dip in Γ at $a/c = 1.225$ for the nominal model, see Figure 4.3.

For event 2 we find that the best fit thermal inertia over all shapes is 4 ± 2 J $s^{-1/2}$ K^{-1} m^{-2} for the nominal axis and 3 ± 2 J $s^{-1/2}$ K^{-1} m^{-2} for the off axis solution. Note that this is a rough on the eye estimate, while a more statistically firm answer would ask for a properly sampled shape distribution. Over the whole range, the nominal axis has a lower reduced χ^2 of $\sim 10 - 20$ % than the off axis model, with the exception of a small fluctuation at $\Gamma \approx 0.5$ J $s^{-1/2}$ K^{-1} m^{-2}.

Chapter 5

Discussion

5.1 Influence of shape

Implementing the new shape model for Patroclus and Menoetius in the eclipse analysis has a profound influence on the thermophysical model, especially for the determination of thermal inertia. The strong dependence of the thermal inertia on shape is clearly visible in Figure 4.3. The fit for thermal inertia varies by approximately a factor of 6 depending on the shape. The beaming parameter, which is an indication for surface roughness, is also strongly dependent on the exact shape model.

Our findings are consistent with the analysis by Hanuš et al. (2015) of the significance of asteroid shape models and pole orientation in thermophysical modeling. They find that a TPM has a strong dependance on variations of the shape model. Uncertainties on best fitting parameters (such as thermal inertia) are usually underestimated if the uncertainty in the shape model is underestimated. The uncertainties in the shape model must therefore be considered in thermophysical modeling.

5.2 Thermal inertia of Patroclus

We find an updated thermal inertia estimate for Patroclus with the new ellipsoid shape model from Buie et al. (2015) of 0.23 ± 0.17 J $s^{-1/2}$ K^{-1} m^{-2} for eclipse event 1 and 1.00 ± 0.45 J $s^{-1/2}$ K^{-1} m^{-2} for eclipse event 2. The previously determined thermal inertia for Patroclus assuming two spherical components by Mueller et al. (2010) was 21 ± 14 J $s^{-1/2}$ K^{-1} m^{-2} for event 1 and 6.4 ± 1.6 J $s^{-1/2}$ K^{-1} m^{-2} for event 2. The updated value for thermal inertia is substantially lower than previously determined, indicating a highly fine-grained and fluffy regolith on the surface.

We see a general trend of lower thermal inertia for more ellipsoid shapes for both events. This is expected, since the longest axes of the components are aligned towards each other, so that the shadow during an eclipse on the eclipsed component is a projection of the smallest cross section of the other component. A more ellipsoid shape will thus have a smaller shadow during the eclipse and cause a shallower eclipse flux drop. The model compensates to fit with the actual data by increasing the eclipse depth, seemingly causing a higher temperature variation, which corresponds to a lower thermal inertia. The underestimation of the eclipse depth thus leads to an underestimation of thermal inertia.

For the lower axis ratio models in event 1 and all shapes in event 2, the thermal inertia for the off axis event is below that of the nominal axis event. This may indicate that the off axis cases have a smaller eclipse depth than the nominal axis cases for the same reason as above.

We see that especially for the nominal case of event 1 the shape model drastically influences the thermal inertia determination. Clearly the shape model has a significant influence on the determination of the thermal inertia in this case. For the other cases the shape varying effect is smaller, but it is still significant for the thermal inertia determination. The strong influence of the shape in the BTPM is surprising, since the shape does not seem to be that drastically different when judged by eye, see Figure 4.2.

The thermal inertia values for the two eclipse events dominantly represent the thermal inertia of the two separate components, given that the thermal inertia determination is mainly based on the temperature variation on the shadowed component. The values of thermal inertia for the two events differ approximately by a factor of 4. But within 1.3 σ the two values are still overlapping. Thus we cannot give conclusive evidence that the thermal inertia is similar and that the two components have similar regolith properties, but we cannot reject this possibility either. Similar surface properties would be expected if the two components are formed out of the same material.

The best BTPM fit for the beaming parameter η ranges from 0.76 to 0.84. It is inversely correlated to thermal inertia. The η parameter is a measure of apparent color temperature and indirectly contains information on surface roughness via thermal beaming. For a perfectly smooth sphere with zero thermal inertia $\eta = 1$. Increasing surface roughness causes η to decrease. The smaller found value of $\eta = 0.76$ is higher than the lunar value of ~ 0.72 (Spencer et al., 1989), which would mean that the surface of Patroclus is less rough than that of the Moon. The higher found value of $\eta = 0.84$ represents even less surface roughness. Note that again the η fit for event 1 nominal axis is highly sensitive for the shape of the model.

The reduced χ^2 values for the BTPM fits may seem quite high, but due to systematic uncertainties in thermal infrared observations, in the asteroid shape and in the thermophysical modeling, it is not uncommon to get large reduced χ^2 values (Delbo et al., 2015).

The minimum χ^2 for event 1 is for all shapes lower than for event 2, so we find a better fit for data of eclipse event 1. At first sight, the χ^2 fit for event 2 in Figure 4.6 seems to find a best fit for a shape around $a/c = 1.1$, which is less elongated than the Buie model. However, we cannot conclude that this is a better fitting shape than $a/c = 1.3$. The Buie observations are far more accurate than our TPM. We suggest that some other parameters connected to the shape or orbit model in our TPM may still be off by a small factor. Event 1 even seems to find a minimum χ^2 or best fit at the spherical model, which we reject for the same reason as with event 2.

Note also that for both events χ^2 is invariably lower for the nominal axis solution of the orbit model than for the off axis model. This does give some confidence that the orbit model is reasonably accurate, which would be an independent validation of the Berthier orbit model solution.

The above thermal inertia for the Buie shape model of Patroclus is the nominal result of this research. If we assume that the model shape variation can be used to find a best fit for the thermal inertia, we find for event 2 that the best fit thermal inertia for Patroclus is 3 to 4 $\pm$ 2 J s$^{-1/2}$ K^{-1} m^{-2}, for the off axis and nominal axis model, respectively. Both values are higher than our nominal values of the Buie model (see Table 4.6), but there is an overlap within 1 σ of the lower of these values with the higher nominal value. However, the errors on this fit are not well defined, given that they are a rough on the eye estimate and given that we did not sample the shape distribution.

This varying shape model is not well constrained by the data for event 1. Perhaps the eclipse for event 1 is shallower than the orbit model predicts, since an overestimated eclipse depth leads to an overestimated thermal inertia. This could explain why the thermal inertia for the event 1 nominal axis model is relatively high for the spherical model, but converges to similarly low values like the other event as the models become more and more elliptical. For those more ellipsoid models the eclipse will be shallower, and better fit the observations. However, conclusive evidence cannot be drawn from this.

Care should be taken in this interpretation of a best fit thermal inertia over all shape models as we do not have a representative sampling of the full shape distribution of the asteroid. This is work for a follow up study. Nonetheless, given that we see a similar trend as in Hanuš et al. (2015) and that there is a partial overlap with our nominal values, we conclude that the minimum that we find in Figure 4.8 is close to the real value of the thermal inertia for Patroclus.

The low thermal inertia of Patroclus is possible given values for other asteroids. Known thermal inertia values for Trojan asteroids range from 7 $\pm$ 7 to 50 $\pm$ 20 J s$^{-1/2}$ K^{-1} m^{-2} (Delbo et al. (2015) and references therein). The new value for Patroclus is low, even for a Trojan, but not unphysical.

Also, thermal inertias for trans-Neptunian objects (TNOs) can be comparably low as for Patroclus. For example the thermal inertia of the TNO 136108 Haumea is 0.3 $\pm$ 0.2 J s$^{-1/2}$ K^{-1} m^{-2} and the thermal inertia of the TNO 90482 Orcus is 1 $\pm$ 1 J s$^{-1/2}$ K^{-1} m^{-2} (Delbo et al. (2015) and references therein). This raises the intriguing question whether Patroclus could be a captured TNO. If so, this would be an important fact for evolution models of our solar system. Any model that tries to explain the formation of the solar system would then have to include a mechanism to migrate TNOs inwards. It would also have to explain the spectral type of Patroclus, which seems to exclude an origin as a TNO.

We do need to keep in mind that thermal inertia is a function of temperature. The thermal conductivity scales with T^3 for predominantly radiative heat transfer between loose grains, so $\Gamma \propto \sqrt{\kappa} \propto T^{3/2} \propto r^{-3/4}$ (see Mueller et al., 2010). At the cold Jovian outskirts the thermal inertia for fine regolith would be approximately 4 times lower than on the Moon. We thus especially need to take extra care when comparing thermal inertia values of objects at different distances from the Sun.

Also, the fitted thermal inertia is an average value over approximately the depth that the heat wave penetrates, including the effects of radiative heat transfer between particles, but not explicitly calculating the radiative heat transfer. We need to keep in mind that not only thermal inertia actually does vary with depth and temperature, but also the particle size and the thermal conductivity vary with depth and temperature.

Another important effect that cannot be neglected is that the value for thermal inertia as determined by the eclipse method is normally lower than with the diurnal method. See for example the values for the Jupiter moons in Table 2.1. This is due to the small duration of an eclipse in comparison to the daily temperature variation. The heat wave thus penetrates the surface less deep and effectively only probes the top surface layer. The top layer is expected to be the finest in structure and have the lowest thermal inertia. This effect needs to be taken into account when comparing thermal inertia values that are determined with different methods. The low thermal inertia of Patroclus that we find may thus be partially due to a vertical grain size sorting, with finer grains on top and increasing particle size with increasing depth.

5.3 Diameter and mass density

Our results for the diameters and mass densities agree with the results from previous studies within the 1-σ level, see the comparison in Table 5.1. The density remains indicative of a loose structure consisting mainly of water ice.

Reference	D (km)	D_1 (km)	D_2 (km)	ρ (g cm^{-3})
Marchis et al. (2006) & Fernández et al. (2003)	166.0 ± 4.8	121.8 ± 3.2	112.6 ± 3.2	$0.8^{+0.2}_{-0.1}$
Buie et al. (2015)	154 ± 4	113 ± 3	104 ± 3	0.88 ± 0.16
Mueller et al. (2010)	154 ± 15	106 ± 11	98 ± 10	1.08 ± 0.33
This work, event 1	154 ± 15	113 ± 11	105 ± 10	0.88 ± 0.26
This work, event 2	152 ± 15	112 ± 11	103 ± 10	0.92 ± 0.26

Table 5.1: Comparison of estimates for area equivalent diameter D, individual asteroid diameters D_1 and D_2 and mean density ρ from different references.

The stellar occultation by Patroclus as observed by Buie et al. (2015) was a direct and accurate observation of the separation distance between the components and their individual sizes. The values for the individual asteroid diameters from Mueller et al. (2010) and this work match within 1 σ with those from Buie et al. (2015).

For the assumption of a spherical model, a mistake in the first analysis of the Patroclus thermal eclipse data by Mueller et al. (2010) is corrected in our validation of these results. The diameter for event 2 is corrected by about 1 %. This is however a small correction considering the systematic errors for the diameter of about 10 %.

Chapter 6

Conclusions

6.1 Role of shape in thermal eclipse models

We conclude that shape is a highly important factor in the thermophysical modeling of eclipse data. In order to successfully perform a thermal analysis of an eclipse, **the shape needs to be known with a high precision**, in particular for the determination of the thermal inertia. And if the shape is not known precisely, the error analysis for the thermal inertia must account for this. Future improvement of thermal analysis techniques thus will need to include improving of asteroid shape models.

6.2 Patroclus

Assuming the ellipsoidal shape as derived by Buie et al. (2015), the value of the thermal inertia that we find is 0.23 $\pm$ 0.17 J $s^{-1/2}$ K^{-1} m^{-2} for eclipse event 1 and 1.00 $\pm$ 0.45 J $s^{-1/2}$ K^{-1} m^{-2} for eclipse event 2. This is much lower than the values found by Mueller et al. (2010), assuming spherical shape, of 21 $\pm$ 14 J $s^{-1/2}$ K^{-1} m^{-2} and 6.4 $\pm$ 1.6 J $s^{-1/2}$ K^{-1} m^{-2}, respectively.

This means that the top surface layer of Patroclus is made up of even finer and fluffier regolith than previously assumed. The overlap between the thermal inertia for events 1 and 2 is too small to conclude that the two components have a similar surface composition, but large enough to consider this possibility. This would be consistent with the idea that the two components were formed from the same cloud of material.

We caution that our error estimates on the thermal inertia for Patroclus do not account for uncertainties in the shape model. The error should therefore be interpreted as a minimum estimate of the real uncertainty in thermal inertia.

The very low thermal inertia for Patroclus is comparable with that of TNOs. While at first sight this suggests that there is a relation between these objects, we also should take into account the different locations in the solar system where these objects reside. The TNOs are at considerably larger distances and have correspondingly lower temperatures. As a result, the average thermal inertia of TNOs is lower. However, it may point to an interesting relationship. In this case, it may suggest an origin of Patroclus in the outer solar system. The low density of 0.88 ± 0.26 g cm^{-3} for event 1 and 0.92 ± 0.26 g cm^{-3} for event 2 indicates a porous structure with a composition of mainly water ice, which would resemble the composition of TNOs and support the idea of a connection of Patroclus to TNOs.

With respect to asteroids in the main belt, we see that most of these have a higher thermal inertia. This implies that these objects have a different surface structure with coarser regolith. However, further research is necessary as we again have to take into account that MBAs are closer to the Sun and thus have a higher temperature. We find no conclusive evidence for an origin of Patroclus as a TNO or MBA, but no counterevidence either.

The origin of Patroclus remains undecided and the surface structure is an important key to better understand its formation. Patroclus is among the targets of the Lucy mission concept, currently under study at NASA. If approved, Lucy will fly by Patroclus in 2033, and should subject our predictions about regolith structure to a thorough observational test.

Chapter 7

Acknowledgements

For the completion of this MSc thesis I owe gratitude to many friends and colleagues. First of all, I would like to thank Migo Mueller, my supervisor, for his firm guidance and encouragements along the way. In particular I'm very grateful for his patience and the many useful comments that have been so essential towards completing this thesis. I'm also grateful to Floris van der Tak for his support and wise recommendations to keep me on track. In the last months Reynier Peletier provided me with a future to look forward to, for which I wish to thank him.

Over the years I enjoyed the friendship and contact with many fellow students. In particular Jorien, Keimpe, Jeffrey, Job, Eva, Ellen, Matthijs and Mathijs have been a great support. Both inside and outside of the Kapteyn Institute, Bernard has been a source of inspiration, help, as well as the source of a neverending sequence of stories.

Outside the Kapteyn Institute, some have played an instrumental role in encouraging me to pursue my study and ambitions. Hens has been very important to keep my feet on the ground. Her friendship and wisdom have given me a solid base for more than a decade. Robert and Nynke are great friends and always take care of many relaxing moments. Mam and dad, thank you for being there, and Evelien for being my lifelong best friend. I also owe Auke for being there in a difficult time and to show how the pursuit of one's ambitions ultimately leads to success. And Rien for his neverending trust, support, help and love.

Last but not least, I should not forget to mention the tremendous role of Bucky and Piep, their unconditional love and friendship gives sunshine and happiness to every day.

Bibliography

J. Berthier, F. Marchis, P. Descamps, M. Assafin, S. Bouley, F. Colas, G. Dubos, J. P. Emery, P. De Cat, J. A. Farrell, A. Leroy, T. Pauwels, J. T. Pollock, V. Reddy, P. V. Sada, P. Vingerhoets, F. Vachier, R. Vieira-Martins, M. H. Wong, D. E. Reichart, K. M. Ivarsen, J. A. Crain, A. P. LaCluyze, and M. C. Nysewander. An Observing Campaign of the Mutual Events Within (617) Patroclus-Menoetius Binary Trojan System. In *AAS/Division for Planetary Sciences Meeting Abstracts #39*, volume 39 of *Bulletin of the American Astronomical Society*, page 482, Oct. 2007.

M. W. Buie, C. B. Olkin, W. J. Merline, K. J. Walsh, H. F. Levison, B. Timerson, D. Herald, W. M. Owen, Jr., H. B. Abramson, K. J. Abramson, D. C. Breit, D. B. Caton, S. J. Conard, M. A. Croom, R. W. Dunford, J. A. Dunford, D. W. Dunham, C. K. Ellington, Y. Liu, P. D. Maley, A. M. Olsen, S. Preston, R. Royer, A. E. Scheck, C. Sherrod, L. Sherrod, T. J. Swift, L. W. Taylor, III, and R. Venable. Size and Shape from Stellar Occultation Observations of the Double Jupiter Trojan Patroclus and Menoetius. AJ, 149:113, Mar. 2015. doi: 10.1088/0004-6256/149/3/113.

M. T. Capria, F. Tosi, F. Capaccioni, M. C. De Sanctis, G. Filacchione, S. Erard, C. Leyrat, and E. Kuehrt. The Thermal Inertia of Lutetia as Derived from VIRTIS/Rosetta. In *Asteroids, Comets, Meteors 2012*, volume 1667 of *LPI Contributions*, page 6391, May 2012.

M. Delbo, M. Mueller, J. P. Emery, B. Rozitis, and M. T. Capria. *Asteroid Thermophysical Modeling*, pages 107–128. 2015.

J. P. Emery, D. M. Burr, and D. P. Cruikshank. Near-infrared Spectroscopy of Trojan Asteroids: Evidence for Two Compositional Groups. AJ, 141:25, Jan. 2011. doi: 10.1088/0004-6256/141/1/25.

J. P. Emery, F. Marzari, A. Morbidelli, L. M. French, and T. Grav. *The Complex History of Trojan Asteroids*, pages 203–220. 2015.

Y. R. Fernández, S. S. Sheppard, and D. C. Jewitt. The Albedo Distribution of Jovian Trojan Asteroids. AJ, 126:1563–1574, Sept. 2003. doi: 10.1086/377015.

J. Hanuš, M. Delbo', J. Ďurech, and V. Alí-Lagoa. Thermophysical modeling of asteroids from WISE thermal infrared data - Significance of the shape model and the pole orientation uncertainties. Icarus, 256:101–116, Aug. 2015. doi: 10.1016/j.icarus.2015.04.014.

J. R. Houck, T. L. Roellig, J. van Cleve, W. J. Forrest, T. Herter, C. R. Lawrence, K. Matthews, H. J. Reitsema, B. T. Soifer, D. M. Watson, D. Weedman, M. Huisjen, J. Troeltzsch, D. J. Barry, J. Bernard-Salas, C. E. Blacken, B. R. Brandl, V. Charmandaris, D. Devost, G. E. Gull, P. Hall, C. P. Henderson, S. J. U. Higdon, B. E. Pirger, J. Schoenwald, G. C. Sloan, K. I. Uchida, P. N. Appleton, L. Armus, M. J. Burgdorf, S. B. Fajardo-Acosta, C. J. Grillmair, J. G. Ingalls, P. W. Morris, and H. I. Teplitz. The Infrared Spectrograph (IRS) on the Spitzer Space Telescope. *ApJS*, 154:18–24, Sept. 2004. doi: 10.1086/423134.

W. A. Hovis and W. R. Callahan. Infrared reflectance spectra of igneous rocks, tuffs, and red sandstone from 0.5 to 22 μ. *J. Opt. Soc. Am.*, 56(5):639–643, May 1966. doi: 10.1364/JOSA.56.000639. URL `http://www.osapublishing.org/abstract.cfm?URI=josa-56-5-639`.

P. L. Lamy, O. Groussin, S. Fornasier, L. Jorda, M. Kaasalainen, and M. A. Barucci. Thermal properties of asteroid 21 Lutetia from Spitzer Space Telescope observations. A&A, 516:A74, June 2010. doi: 10.1051/0004-6361/201014361.

F. Marchis, D. Hestroffer, P. Descamps, J. Berthier, A. H. Bouchez, R. D. Campbell, J. C. Y. Chin, M. A. van Dam, S. K. Hartman, E. M. Johansson, R. E. Lafon, D. Le Mignant, I. de Pater, P. J. Stomski, D. M. Summers, F. Vachier, P. L. Wizinovich, and M. H. Wong. A low density of 0.8gcm^{-3} for the Trojan binary asteroid 617Patroclus. Nature, 439:565–567, Feb. 2006. doi: 10.1038/nature04350.

J.-L. Margot, P. Pravec, P. Taylor, B. Carry, and S. Jacobson. *Asteroid Systems: Binaries, Triples, and Pairs*, pages 355–374. 2015.

F. Marzari, H. Scholl, C. Murray, and C. Lagerkvist. *Origin and Evolution of Trojan Asteroids*, pages 725–738. Mar. 2002.

W. J. Merline, L. M. Close, N. Siegler, D. Potter, C. R. Chapman, C. Dumas, F. Menard, D. C. Slater, A. C. Baker, M. G. Edmunds, G. Mathlin, O. Guyon, and K. Roth. S/2001 (617) 1. IAU Circ., 7741, Oct. 2001.

A. Morbidelli, H. F. Levison, K. Tsiganis, and R. Gomes. Chaotic capture of Jupiter's Trojan asteroids in the early Solar System. Nature, 435:462–465, May 2005. doi: 10.1038/nature03540.

D. Morrison and D. P. Cruikshank. Thermal Properties of the Galilean Satellites. Icarus, 18:224–236, Feb. 1973. doi: 10.1016/0019-1035(73)90207-8.

M. Mueller. Surface Properties of Asteroids from Mid-Infrared Observations and Thermophysical Modeling, PhD thesis. *ArXiv e-prints*, 2007.

M. Mueller, F. Marchis, J. P. Emery, A. W. Harris, S. Mottola, D. Hestroffer, J. Berthier, and M. di Martino. Eclipsing binary Trojan asteroid Patroclus: Thermal inertia from Spitzer observations. Icarus, 205:505–515, Feb. 2010. doi: 10.1016/j.icarus.2009.07.043.

C. Neese. Asteroid Taxonomy V6.0. EAR-A-5-DDR-TAXONOMY-V6.0. *NASA Planetary Data System*, 2010.

G. Neugebauer, K. Matthews, P. D. Nicholson, B. T. Soifer, I. Gatley, and S. V. W. Beckwith. Thermal response of Iapetus to an eclipse by Saturn's rings. Icarus, 177: 63–68, Sept. 2005. doi: 10.1016/j.icarus.2005.03.002.

L. O'Rourke, T. Müller, I. Valtchanov, B. Altieri, B. M. González-Garcia, B. Bhattacharya, L. Jorda, B. Carry, M. Küppers, O. Groussin, K. Altwegg, M. A. Barucci, D. Bockelee-Morvan, J. Crovisier, E. Dotto, P. Garcia-Lario, M. Kidger, A. Llorente, R. Lorente, A. P. Marston, M. Sanchez Portal, R. Schulz, M. Sierra, D. Teyssier, and R. Vavrek. Thermal and shape properties of asteroid (21) Lutetia from Herschel observations around the Rosetta flyby. Planet. Space Sci., 66:192–199, June 2012. doi: 10.1016/j.pss.2012.01.004.

J. C. Pearl, M. S. Kaelberer, M. E. Segura, J. R. Spencer, and C. Howett. Eclipse Measurements of Saturn's Moons from Cassini CIRS. In *AAS/Division for Planetary Sciences Meeting Abstracts #40*, volume 40 of *Bulletin of the American Astronomical Society*, page 510, Sept. 2008.

E. Pettit and S. B. Nicholson. Lunar radiation and temperatures. ApJ, 71:102–135, Mar. 1930. doi: 10.1086/143236.

R. Schulz, H. Sierks, M. Küppers, and A. Accomazzo. Rosetta fly-by at asteroid (21) Lutetia: An overview. Planet. Space Sci., 66:2–8, June 2012. doi: 10.1016/j.pss.2011.11.013.

J. R. Spencer. A rough-surface thermophysical model for airless planets. Icarus, 83:27–38, Jan. 1990. doi: 10.1016/0019-1035(90)90004-S.

J. R. Spencer, L. A. Lebofsky, and M. V. Sykes. Systematic biases in radiometric diameter determinations. Icarus, 78:337–354, Apr. 1989. doi: 10.1016/0019-1035(89)90182-6.

E. F. Tedesco, P. V. Noah, M. Noah, and S. D. Price. The Supplemental IRAS Minor Planet Survey. AJ, 123:1056–1085, Feb. 2002. doi: 10.1086/338320.

D. Vokrouhlický, W. F. Bottke, S. R. Chesley, D. J. Scheeres, and T. S. Statler. *The Yarkovsky and YORP Effects*, pages 509–531. 2015.

M. W. Werner, T. L. Roellig, F. J. Low, G. H. Rieke, M. Rieke, W. F. Hoffmann, E. Young, J. R. Houck, B. Brandl, G. G. Fazio, J. L. Hora, R. D. Gehrz, G. Helou, B. T. Soifer, J. Stauffer, J. Keene, P. Eisenhardt, D. Gallagher, T. N. Gautier, W. Irace, C. R. Lawrence, L. Simmons, J. E. Van Cleve, M. Jura, E. L. Wright, and D. P. Cruikshank. The Spitzer Space Telescope Mission. *ApJS*, 154:1–9, Sept. 2004. doi: 10.1086/422992.